Effect of De-convoluted Rise Times in Mass Composition Studies with the Surface Detectors of the Pierre Auger Observatory

Pierre Erwan Saouter

Pour le Titre de Master en Physique des Particules
University of Geneva

May 2009

Acknowledgments

The five months I spent in Argentina, in the group of the National University of La Plata (UNLP), were a most instructive and rewarding experience. This unique chance was only possible thanks to the conjoint help of many people to whom I shall now present my sincere acknowledgments.

I would first like to thank Hernan Wahlberg, my supervisor in Argentina. It would be impossible to tell how much I learn working under his supervision without being incomplete. He always took the time needed to help me solve the problems encountered in my work. Through his unique way of seeing and explaining physics, he gave me a whole new understanding of cosmic ray physics and the challenge of experimental physics in general. The satisfaction of the work accomplished for this thesis only comes with the recognition of his contribution to it. More than a supervisor, Hernan was also a great friend who I must thank again for all the practical help he gave me during my stay in this foreign country from which I did not speak the language.

My stay in Argentina could have never been so successful without the two professors Maria Teresa Dova and Martin Pohl. Without their support, as much administrative than personal, this experience would have never taken place. We sincerely hope this first successful exchange program will lead to a future collaboration between both universities.

I must thank the rest of the group of La Plata for their kindness and presence, making the everyday life easier and happier. More than the help in my work, I was overwhelmed by the profound human dimension I was surrounded by. Fernando, Flavia, Analisa and Luis, thank you very much.

Not a physicist but not less the best friend I met during my trip, thank you for all the great moments Irene!

Abstract

It has been almost a century since cosmic rays were first discovered and yet the origins, production and acceleration mechanisms of these particles at the highest energies are not perfectly understood. Above 10^{20}eV, all possible species of cosmic ray particles, except neutrinos, interact strongly with the cosmic ray background and hence their flux should be strongly suppressed, except for those whose sources are sufficiently close to the earth on a cosmological scale (distances smaller than 100 Mpc). Furthermore, the basic requirements which must be met by astrophysical objects to accelerate particles to energies greater than 10^{19}eV are not easily met. At present, no conclusive source identification for these particles have been obtained.

Identifying the sources of high energy cosmic rays would be easier and more efficient if we were to know the primary composition of these particles. Considering models of the magnetic fields in our galaxy and its surrounding, information on mass composition would allow for corrections in the arrival directions of cosmic rays. However, composition of cosmic rays at the highest energies is very poorly known. Therefore many techniques and studies have been developed in the recent years. Using the asymmetry in the arrival time distribution of particles at ground, the group of the National University of La Plata (UNLP) has developed a novel and very promising technique for mass composition estimations.

Applying this method to the Pierre Auger Observatory data, the question wether the time distributions should be previously corrected from any detector effects has been raised. In this work, we have tested the effects of corrected time distributions on the asymmetry method, using a suitable deconvolution procedure. It is shown that unexpected effects are observed in the different steps of the analysis but that the final result on mass composition remains compatible, within errors, for the detected signals and the corrected ones.

To Mélanie,
without whom I could have walked through life without knowing what love is truly about.

Contents

Chapter 1

Ultrahigh Energy Cosmic Rays at the Pierre Auger Observatory

Ultra High Energy Cosmic Rays (UHECRs) are known as those particles that hit the earth's atmosphere at energies above 10^{18} eV. Such energies have opened the question of their sources and mechanisms of production. After more then 80 years of research in cosmic ray physics, the answer to these questions have not yet been given. This is known as the enigma of the highest energy cosmic rays.

Even at energies of 10^{14}eV, cosmic rays are too rare to be measured efficiently by instruments carried by balloons or spacecrafts and their detection relies on the extensive air showers (EAS) produced in the earth atmosphere. The components of these EAS can be detected at ground level and features such as the energy and the arrival direction of the primary cosmic ray can be inferred. The detection of UHECRs implies using the largest detection areas possible. With it's final inauguration in november 2008, the Pierre Auger Observatory (PAO) is now the largest detector in the world, with a detection area spread over nearly 3000 km^2.

In this chapter, we review briefly the main ingredients of cosmic ray physics, concentrating on the enigma of UHECRs and the way the PAO aims to address this issue. We also present the first results published by the Pierre Auger Collaboration. We do not give here an introduction to cosmic ray physics and its history. For more information on this subject, we recommend the excellent review by M. Nagano and A. A. Watson [1] and the very complete reference [2]. See also reference [3] for a detailed discussion of high energy physics in the atmosphere.

1.1 The Energy Spectrum of Cosmic Rays

One of the easiest way to summarize todays understanding of cosmic rays is to discuss their well-known energy spectrum. Figure 1.1 shows one of the latest result for this spectrum, obtained by grouping data from different experiments.

Under 10 GeV, the flux is modulated by the solar wind. Above this energy, the rest of the spectrum is well described by a power law of the form

$$\frac{dN(E)}{dE} \propto E^{-\gamma} \tag{1.1}$$

where N holds for the number of particles. The index γ must change over certain ranges of energy to represent correctly the features of the observed flux. At 5 PeV, there is a steepening from $\gamma \sim 2.7$ to $\gamma \sim 3.1$ in the spectrum, this feature being known as the first *knee*. A second knee appears around 400-500 PeV where the index reaches a value of ∼3.3. However, at very high energies of $\sim$ 4 EeV, the spectrum flattens again, γ being around 2.7, a region called the *ankle*. These features of the spectrum have been studied independently by several experiments. It is believed these changes are due to differences in the production and propagation mechanisms involved at the different energies. For instance, the steepening in the spectrum from $\gamma \sim 2.7$ to $\gamma \sim 3.1$ was studied by the KASKADE experiment [4] and it was found that the change in spectral index is due to the progressive hardening in the spectra of individual elements with mass below carbon.

The two great questions about the highest energy cosmic rays concern their origin and acceleration mechanisms. Several explanations have been put forward to try to describe where and how cosmic arrays above the knee reach such energies. Some models predict other galactic sources to cosmic rays than supernovae remanent (SNR), such as Type II supernovae or gamma ray bursts. It is postulated that these events occur with a sufficiently high frequency to create particles with energies up to the ankle. Above this limit, the flux becomes dominated by its extragalactic component. Others think this transition actually occurs at the second knee and the ankle characteristic is the result of e^+e^- pair production caused by a spectrum dominated by protons interacting with the cosmic microwave background (CMBR):

$$p + \gamma_{CMBR} \longrightarrow p + e^+ + e^- \tag{1.2}$$

As the change in the average mass at the ankle should be different for the two scenarios, it should be in principle possible to discriminate these two rival explanations by using mass composition measurements . If the transition

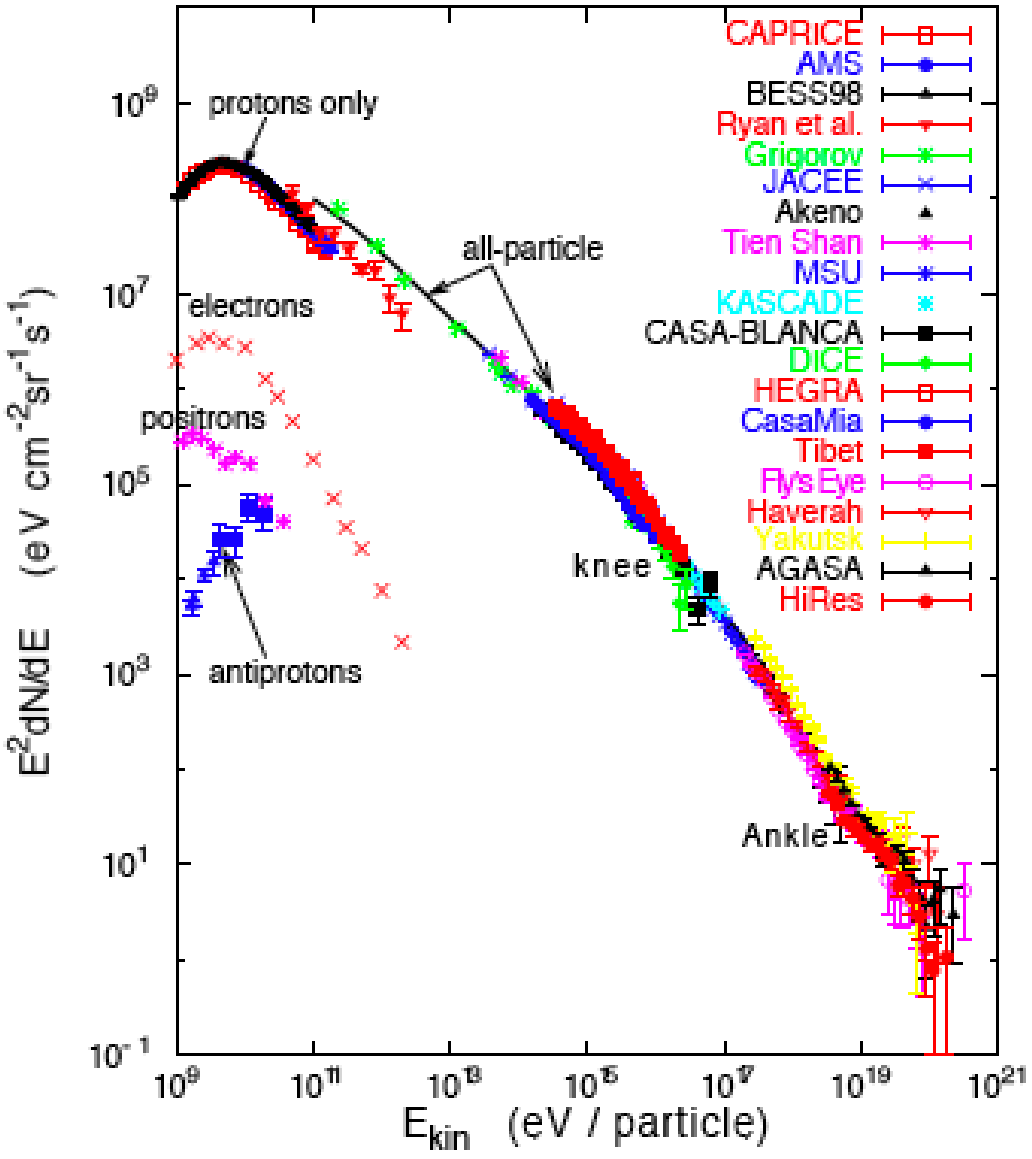

Figure 1.1: *Energy flux spectrum of cosmic rays obtained by different experiments. The features of both knees and the ankle can clearly be observed.*

model is correct, the composition under the ankle is expected to be dominated by iron. On the contrary, if the ankle is due to pair production from interaction with the CMBR, then the flux should be dominated by protons.

Above the ankle (4 EeV), cosmic rays are most probably of extragalactic origin. The flux being very low, direct measurements of the spectrum become impossible. To get a better idea, the number of events are estimated of the order of 100 $\mathrm{km}^{-2}\mathrm{y}^{-1}$ for 1 EeV, 1 $\mathrm{km}^{-2}\mathrm{y}^{-1}$ for 10 EeV and 1 km^{-2} per century for 100 EeV.

1.2 The GZK Cut-Off

There are many processes that can degrade the energy of particles as they travel through the cosmos [5]. In addition to energy losses caused by the interaction with the CMBR and the production of electron/positron pairs, UHE protons undergo other processes such as Hubbles expansion and interaction with dust. Still, for proton primaries, the most important process of energy loss is the mechanism of photo-pion production by interaction with the CMBR:

$$p + \gamma_{CMBR} \longrightarrow \Delta^{+} \longrightarrow p + \pi^{0} \quad or \quad n + \pi^{+} \tag{1.3}$$

This interaction is expected to provoke a steepening of the spectrum between 40 and 70 EeV if the flux is dominated by protons, corresponding to the well-known GZK cutoff, from its co-discoverers Greisen, Zatsepin and Kuz'min. This limits the average propagation distance of the protonic component of UHECR above $\sim$ 50 EeV to 100 Mpc. On this basis, the "GZK horizon" is defined as the radius of a sphere containing all the sources producing 90% of the UHECRs arriving above a certain energy threshold. Assuming an isotropic distribution of the sources with same intensities and spectral index, the GZK horizon is 200 Mpc and 80 Mpc for energies of 60 EeV and 80 EeV respectively. If the GZK modulation was to be observed, this would thus suggest that the sources of UHECRs observed on earth are localized between 80 and 200Mpc, a distance cosmologically close to earth.

For heavier elements than protons, where the constituent nucleons share the energy of the primary, the essential mechanism of energy loss at energies above 10^{19}eV is photodesintegration by interaction with the "Extragalactic Background Light" (EBL) or the CMBR:

$$N^{A} + \gamma_{CMBR} \longrightarrow N^{A-1} + p \quad or \quad n \tag{1.4}$$

The typical energy loss distance of an iron nucleus at 10^{20}eV via this process is 100 Mpc, thus similar to the one for protons. Therefore, if a steepening in the spectrum is observed at 50EeV, this would not necessarily indicate a change in mass composition of particles accelerated by sources between 10^{19} and 10^{20}eV, i.e., changes in the spectrum at the highest energies may not be an indication of changes in the mass composition. Further, if iron contributes significantly to the flux at 10^{20}eV, it would be expected that the sources be inside a 100 Mpc region of the solar system. In the range 10^{18}-10^{19}eV, the energy losses are equally shared between photodesintegration and the Hubble expansion with a constant rate. Thus, if the flux of cosmic rays at these energies is dominated by iron, accelerated by a unique group of sources, i.e., there is no galactic to extragalactic transition, we would not expect to observe the ankle.

With its unprecedented level of statistics at the highest energies, the Pierre Auger collaboration has recently published a paper claiming the observation of the GZK cutoff [6]. Figure 1.2 shows the results for the differential flux as a function of energy (upper panel) and the fractional differences between Auger and HiRes data [7] with a spectrum with an index of 2.69 (lower panel). These results rely on 661 measured UHE events. We see that around $10^{19.6}$eV, a steepening of the spectrum occurs, as expected from the predictions for the GZK cutoff (this cutoff being theoretically estimated at $5\text{x}10^{19}$ eV).

1.3 The Fermi Acceleration and the Origin of UHECRs

Where and how the highest energy cosmic rays are produced are the main questions of todays cosmic ray physics. The existence of cosmic rays at extreme energies is indisputable and the observed GZK suppression implies the sources of these particles are nearby on a cosmological scale. But even before addressing the question of the origin of UHECRs, the question of the physical mechanisms involved for the acceleration to such energies must be discussed. At the time of the discovery of the most energetic cosmic rays, very few astrophysical mechanisms were known to be able to explain such energies. This unknown led to a very abundant literature of more or less exotic theories. An exhaustive list is given in [8]. The solution proposed by Fermi remained the most convincing and probable explanation.

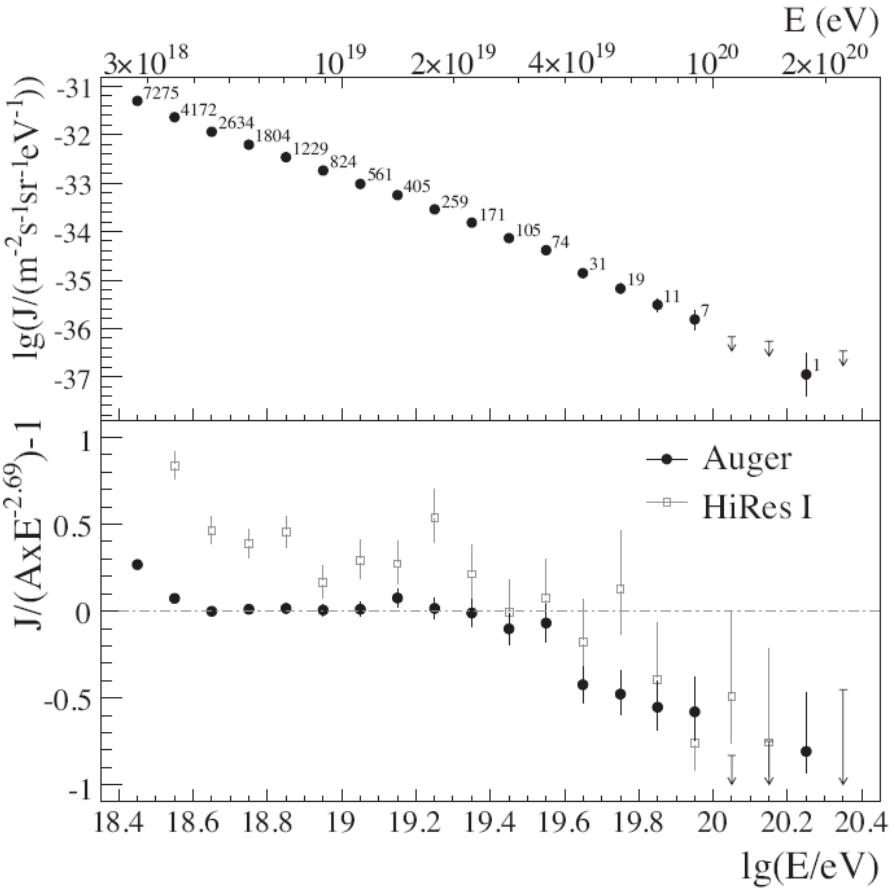

Figure 1.2: *Upper panel presents the differential flux J with energy. The suppression above* 5×10^{19} *is clear. The lower panel shows the difference between two different results and an assumed 2.69 spectral index, both for the Auger and HiRes experiments. The figure taken from [6]*

.

In 1949 [9], Fermi developed a model where particles could achieve very high energies through repeated encounters with moving magnetized plasmas (through a head on collision). The idea is that considering the geometry of dynamic plasma clouds, a particle always gets a positive gain of energy through each encounter, this gain being proportional to its own energy, $\Delta E = \alpha E$. If the initial energy of the particle is E_0, then after k encounter we have $E = E_0(1+\alpha)^k$. What is most interesting is that, considering the escape probability of the accelerated particles, the Fermi mechanism naturally produces a power-law spectrum for the energies of cosmic rays. Furthermore, the Fermi mechanism has already been observed for protons accelerated by the solar wind in the heliosphere [10].

The maximum energy that can be achieved this way usually depends on the time length particles interact with the plasma, which depends on the escape probability of the particle but also on the life time of such plasmas. Very simple models of Fermi acceleration by shock waves [5, 11, 12] show the maximum energy is given by:

$$E_{max} \approx \beta c \times Ze \times B \times L, \tag{1.5}$$

where βc represents the shock velocity, L the characteristic size of the acceleration region, B the magnetic field embedded in the plasma and Ze the charge of the accelerated particle. Equation 1.5 essentially states that the gyromagnetic radius of a Fermi accelerated particle is contained within the acceleration region. Considering a more detailed approach of the shock mechanism and the magnetic environment, it was shown the maximum energy should be reduced by a factor of ten compared to equation 1.5. However, equation 1.5 allows to constraint the possible astrophysical candidates capable of accelerating a particle to such extreme energies of 10^{20}eV through Fermi acceleration. This is shown is Figure 1.3 where the candidates are selected in terms of their magnetic and size properties. Objects below all the diagonal lines are not appropriate to accelerate particles to extreme energies through a Fermi acceleration process. These diagonal lines hold for different cases, the dashed one being for iron nuclei and the solid one for protons. However they correspond to predictions using a $\beta = 1$ value which is extreme. The shaded region above the solid line represents a $\beta = 1/300$ case for protons.

It is very interesting to note that the most powerful accelerators seem to have a maximum energy limit around the GZK cutoff. On another hand, as for any dynamic plasma and magnetic configuration, the maximum energy that is achieved for a nuclei is Z times higher than for a proton, measurements of cosmic rays at the highest energies (above 10^{19}eV) should be most revealing on the potential astrophysical sources. It was shown that large

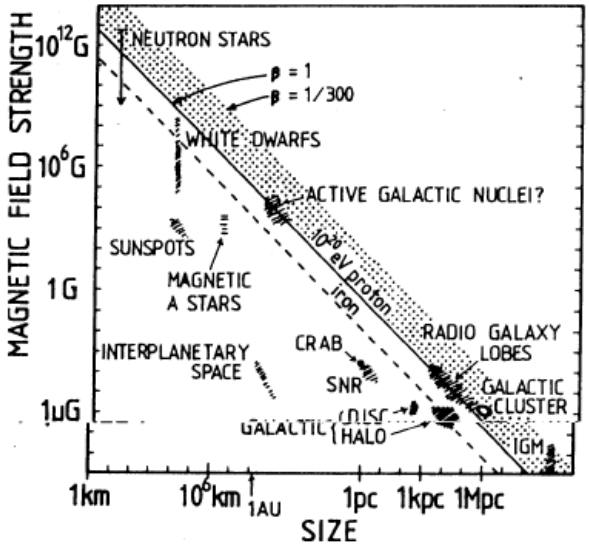

Figure 1.3: *The plot shows which astrophysical candidates have the basic size and magnetic field strength requirements for accelerating particles to extreme energies through Fermi acceleration (see text for more details). Picture is taken from [13]*

.

astrophysical structures such as galaxies or group of galaxies respect the criteria of size and field strength required, and thus merit consideration as potential acceleration sites. It must be said that the extreme energies we are looking for are almost impossible for most of the astrophysical objects presented in Figure 1.3 if we consider the simple model of equation 1.5. Many processes of energy loss must be considered, such as synchrotron radiation, photo-production interactions, etc. Detailed studies showed that compact objects with large magnetic fields, such as neutron stars or Active Galactic Nuclei (AGNs) are the most promising candidates allowing accelerations up to energies greater than 10^{20} eV. More exotic mechanisms (so-called "topological defects") involving unknown and unconventional objects have also been considered. If they were to contribute to the production of cosmic rays, then measurements of UHECRs would have the potential to teach us about new physics. However, recent results have constrained very tightly the limits on the neutrino and photon [14, 15] contributions at ultra-high energies, excluding at the same time most exotic scenarios.

The PAO has recently reported a correlation of the highest energy cosmic rays with AGNs [16]. The main plot illustrating this result is presented in

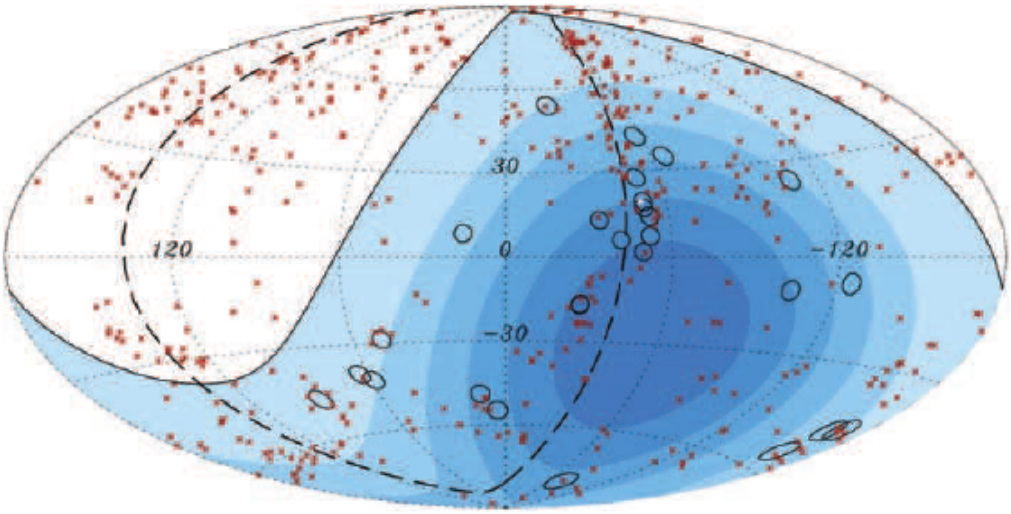

Figure 1.4: *Projection of the 27 highest energy events (> 56 EeV) used for establishing a correlation with AGNs (red dots). The events are represented by the black circles, defining a 3.2° field around each event. Dashed lines indicate the super-galactic plane and the shading represents the exposure of different regions of the sky to the PAO. The picture is taken from [18]*

.

Figure 1.4. The 27 events with energies above 56 EeV used here are represented by the black circles which define a 3.2° field around the reconstructed location of these events. The red dots represent a catalogue of 442 AGNs. The anisotropy of events with these extreme energies is clear and considering a 3.2° angular field for each events, a correlation with AGNs at distances closer than 75 Mpc seems to appear. It was calculated that assuming an isotropic distribution of events in the sky, the probability of observing the correlation by chance is of the order of 1.7×10^{-3}. The statistical and probabilistic interpretation of this result is very complex and still subject to many cross-checks using the data from previous experiments[1]. For more information we recommend the main paper [16] and reference [18].

1.4 Mass Composition of Cosmic Rays

The observation of the flux suppression at the energy predicted for the GZK-effect (Figure 1.2), combined to the AGN correlation measurement, suggests that the sources of events with energies above 56 EeV are located within

[1]For example the re-analysis of the HiRes data [17]

the GZK horizon for protons. Recalling the discussion from section 1.2, this would suggest that the GZK modulation is indeed present and proton dominated. But it is was shown [19] that predictions for composed fluxes of He, CNO, Si and iron nuclei can also fit well the data. However such a composition would be in disagreement with the anisotropy present in the upper end of the spectrum of cosmic rays.

Although the origin and production mechanisms of UHECRs are the main issues of cosmic ray physics, it has become evident that the answers to these questions also require a deeper understanding of the nature of cosmic rays. In the recent years, strong efforts have been made to develop methods to measure the mass composition of cosmic rays at the highest energies. As we have seen, resolving this unknown would strongly support (or not) the first results on the AGN correlation observed at the PAO. If the mass composition of cosmic rays at the highest energies could be determined, then it would also offer a possibility for correcting the reconstructed arrival directions of UHECRs from the deflections the particles undergo when traveling through galactic and extragalactic magnetic fields (assuming the models describing these fields are sufficiently accurate).

Chapter 2

Detection Techniques at the Pierre Auger Observatory

Currently, two methods are used to detect extensive air showers at ground level. The most common one consists in using a set of particle counters spread across a large area to detect directly the secondary particles of the EAS which survive to the detection level. From the recorded densities of particles, information on the energy and arrival direction of the primary particle can be extracted. The second method exploits the fluorescence emission of light in the 300-400nm band induced in the excitation of nitrogen molecules by particles of the shower. The profile of the shower can then be inferred rather directly from the detected light. In this chapter we will review the basic description of these methods considering the specific arrangement of the Pierre Auger Observatory. The particularity of the PAO is that it uses for the first time both detection techniques, enabling measurements in a hybrid mode, improving considerably the accuracy of the reconstructed energy and arrival direction of the primary cosmic particle.

2.1 Detection with Ground Arrays

2.1.1 The Pierre Auger Surface Array

A cosmic ray entering the atmosphere produces a large number of secondary particles spread over a considerable area at the detection level. Surface arrays of detectors are the most common experimental set-up to detect these secondary particles. For ultra high energy cosmic rays, the fluxes are extremely low and only increasing the detection area can improve statistics. With an array of 1600 surface detectors spread over approximately 3000km^{2}m, the

Pierre Auger Observatory is at present the largest detector ever built. Located around the town of Malargüe, in the province of Mendoza, Argentina, the PAO views the southern hemisphere of our galaxy. A second Pierre Auger Observatory is already under construction in the northern hemisphere (Lamar, Colorado) allowing soon a complete cover of the sky. A schematic of the whole set-up of the southern site is shown in Figure 2.1. The surface stations are separated by 1.5 km and 4 fluorescence detector stations are located at the edges of the array, each of them consisting in six mirrors with different fields of view. To detect cosmic rays above 10^{19}eV, arrays are usually built between 800 g.cm^{-2} depth of atmosphere and sea level. This is because the average maximum depth of showers induced by primaries with such energies is about 750 g.cm^{-2} and it is more usefull to study showers close to or beyond the shower maximum (see Chapter 3). The surface array of the PAO is at an average altitude of 1400m which is equivalent to an atmospheric depth of 870 g.cm^{-2}.

The surface detectors were chosen to be water C̃erenkov detectors. Each detector consists of a 1.55 meters high and 3.6m in diameter tank for a surface area of approximately 10 m^2. The tank is filled with 12 tonnes of highly purified water. An advantage of the deep water C̃erenkov technique lies in its ability to respond to the large number of photons of relatively low energy (less than 10 MeV) present in the shower. Furthermore, the assembly cost is lower compared to scintillators although they are more difficult to deploy over large areas. The exposure is also increased for the C̃erenkov detectors as the zenith angles that can be monitored increase from 60° to 80°, allowing specific neutrino studies for very inclined showers. The interior of each tank is covered with a highly reflective TYVEX surface. The light produced by particles traversing the tanks are collected by three 9-inches photomultipliers (PMTs), the output signal of a station being usually an average of the signals measured by each PMT.

At the detection level, most particles of the shower are photons, electrons and muons. The two charged components create C̃erenkov light when they enter the tanks with velocities greater than the speed of the light in the water. The C̃erenkov photons are reflected on the highly-reflective interior covering and collected by the PMTs. As for photons of the shower, they are observed indirectly by the secondary electrons produced via pair-production and Compton scattering, which produce the necessary C̃erenkov light for their detection.

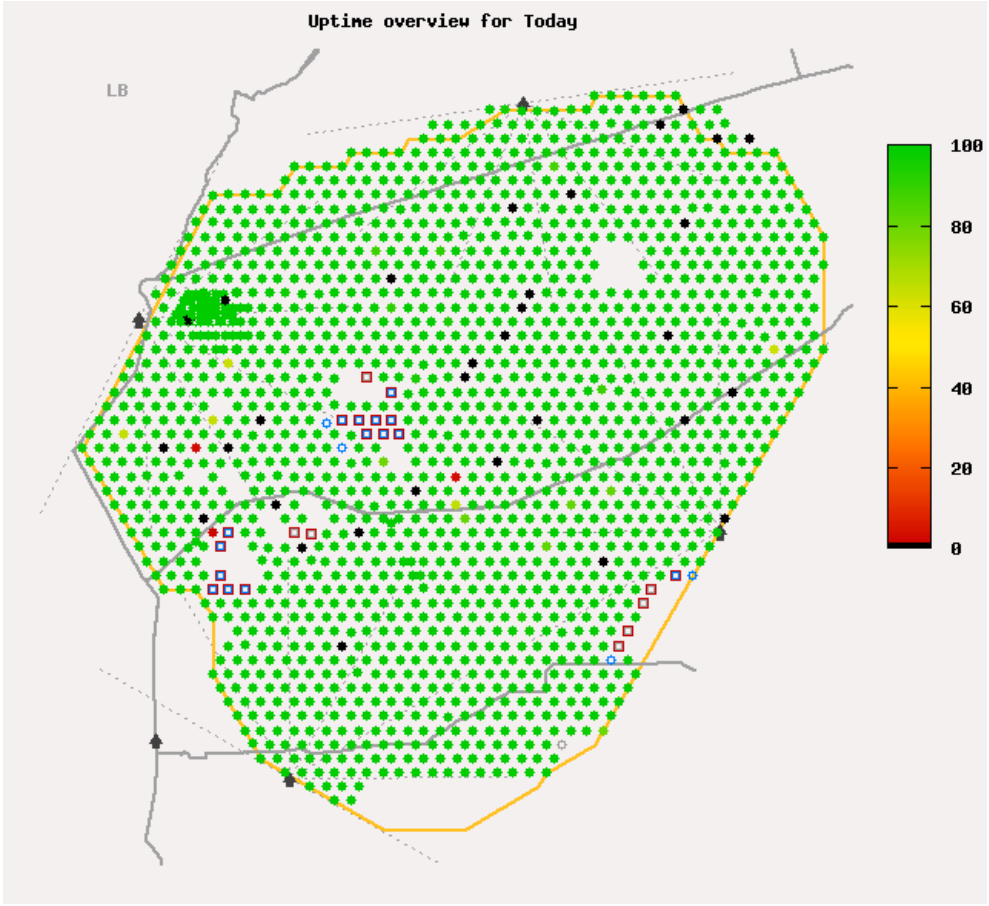

Figure 2.1: *Schematic picture of the whole Pierre Auger Observatory instrument. The colored dots represent the surface detectors, at present at the number of 1600. However, the color is applied to differentiate operating stations (green) from non-operating ones (black). The open squares stand for stations already deployed but not yet equipped with the radio communication system and not yet filled with water. The grey "huts" represent the different transmission antennas.*

2.1.2 Calibration of the Surface Detectors

The surface detectors of the Pierre Auger Observatory are calibrated using the abundant muonic background. The chosen unit of reference (normalization) is the energy deposited by a muon traversing the centre of a tank vertically. This unit is called *Vertical Equivalent Muon* (VEM) and corresponds to an energy deposit of 240 MeV. In each detector there is an automatic conversion from the signals in the FADC channels to signals in VEM. The calibration then consists on verifying that a 1VEM signal is associated to the same deposit in energy for each detector. The signal for a given station is the resulting average of the output signals of the three PMTs converted in units of VEM. This calibration is carried out constantly on a minute scale.

The triggering system of the surface detectors of the array corresponds to a five-stage trigger criteria. The two first levels, the T1 and T2 criteria, are performed locally in each station of the array. They mainly use adjustments in the chosen gain for the PMTs in order to assure a constant trigger rate and establish signal thresholds to identify inclined showers with *Signal Threshold Cuts* (STCs) and cases of saturated stations with a *Time-over-Threshold* (ToT) trigger criteria. Nearly half of the showers with energies above 30 EeV induce saturated signals in stations close to the core of the shower ($\leqslant$600m). Many methods have then been successfully developed to estimate the true signal, extending the possible measurements from 1000 VEM to 10^6 VEM.

The remaining trigger levels are executed from the Central Data Acquisition System (CDAS) located in the main control center of the observatory. The T3 level selects correlated signals (at least 3 T2 stations), both in space in time, from a detected shower. CDAS records the data of the whole array for an event passing this criteria. Further cuts are applied offline, mainly to select events suitable for an accurate reconstruction of the shower parameters: the core location of the shower (and thus the arrival direction of the primary), the S(1000) parameter and the energy (see 2.1.3) . The T4 trigger level for vertical events requires that at least 3 ToT stations are arranged in one of the configurations shown in Figure 2.2. For inclined events which are a combination of SCTs and ToTs, at least 4 stations must pass the T4 criteria and correspond to one of the configuration shown in Figure 2.3.

Finally we have the T5 trigger criteria, which was most important during the construction of the surface array as it rejected events recorded in regions of the array that were not yet completed or with non-operating stations. Now the array is complete, this criteria still applies to stations on the edges of the array or when technical support needs to be brought to some stations.

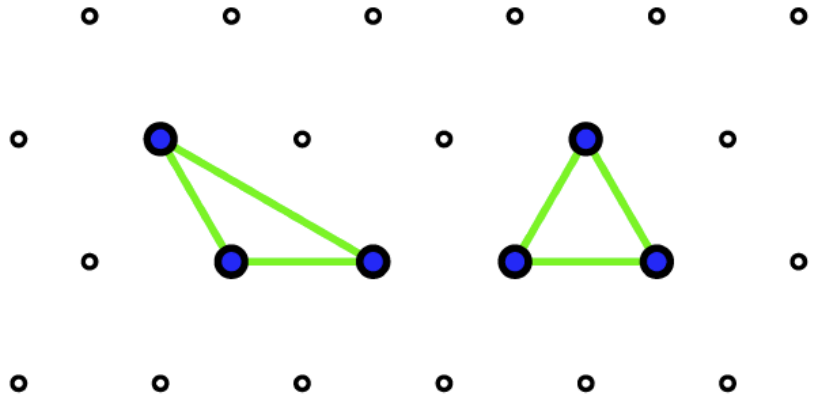

Figure 2.2: *The T4 criteria for vertical events basically requires the three neighbor stations to form a triangular grid.*

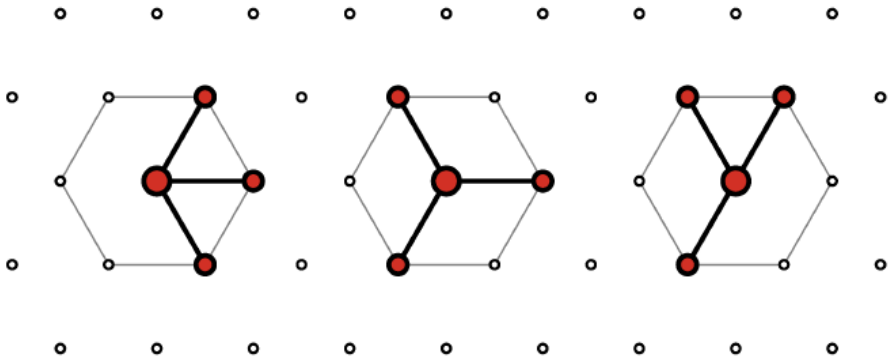

Figure 2.3: *4C1 configurations obeying T4 criteria for inclined events.*

2.1.3 Shower Parameters Reconstruction with SD Measurements

The three essential informations one wants to recover when measuring a EAS is the arrival direction of the primary particle, its energy and the primary composition. Measuring the composition of the primary particle using terrestrial detectors is very difficult, far more than energies and directions. This question being the center of this work, we discuss in detail the problem of mass composition measurements in Chapter 3. We concentrate here on the energy and the arrival direction.

By measuring the relative arrival times of signals at a minimum of three non-collinear detectors, the direction of the shower axis and hence of the primary cosmic ray can be deduced. The arrival times are assigned to the signals by the GPS units of each station. As a first approximation the shower front is assumed to be planar and an initial estimation of the shower direction is made by fitting this planar front which is assumed to be traveling at the velocity of light. Estimating the shower axis is the first step towards finding the core location of the shower at ground. This one is estimated using a maximum likelihood procedure in the fit of an assumed *Lateral Distribution Function* (LDF). The LDF consists in a formal description of the fall-off of particle densities (or alternatively the corresponding signal sizes) of a shower at the detection level with the distance from the shower core. The LDF function must be assumed in this procedure and strong uncertainties on the core location estimation result from uncertainties in the form of the LDF and intrinsic fluctuations in the development of air showers. However, Hillas [20] proposed a solution to this problem, using the signal at a specific distance from the shower core to classify the size of the shower and hence its primary energy. He showed that at an optimum core distance, r_{opt}, the fluctuations in the expected signal, $S(r_{opt})$ are minimized. At the PAO, a NKG-type[1] function is used for the LDF:

$$S_p(r,\beta) = k(\frac{r(m)}{700})^{-\beta}(1+\frac{r(m)}{700})^{-\beta} \tag{2.1}$$

β is the characteristic steepness of the function and r the distance from the shower core. For a triangular configuration of detectors separated by 1500 m, the optimum distance was found to be close to 1000m. One must know that this optimum parameter must be evaluated precisely for each individual shower. Furthermore, the presence of saturated tanks in an event was shown

[1]From its authors Nishimura, Kamata and Greisen.

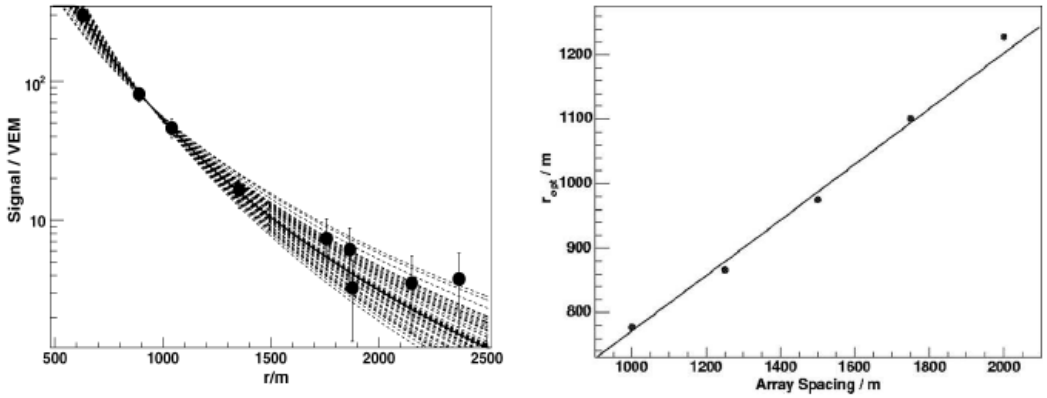

(a) (b)

Figure 2.4: Figure *a) shows the reconstruction of an event using the LDF of equation 2.1, using 50 different values of the slope parameter β. We see that the fluctuations are the smallest around 1000m from the core which is chosen as the optimum distance r_{opt}. b) shows the behavior of r_{opt} as a function of the spacing between the stations of an array. This spacing is of 1500 m for the PAO. Plots are taken from [18]*

to have a significant effect on the r_{opt} parameter and a special treatment is adopted for these cases, see [21]. The results of this study are shown in Figure 2.4. The signal size at 1000 m from the core, $S(1000)$, was establish as the best estimator of the shower size measured with the array of the PAO. With the $S(1000)$ parameter and the core location of a given shower, the assumption of a planar shower front can be modified and a more precise estimation of the arrival direction obtained. Showers with a spherical front with a radius of several kilometers are found to reproduce well the measured densities.

Finally, the size parameter is linked to the energy of the primary particle. Most interesting is the fact that, whereas previous experiments could only calibrate the size estimator of the showers to Monte Carlo simulations, introducing important systematic uncertainties due to the choice of the interaction model, the PAO performs a much more efficient calibration using the calorimetric energy measurement from the fluorescence detectors for a small number of hybrid events. The systematic uncertainties are reduced by 22% and a more precise estimation of the energy of the shower can be made.

2.2 Detection with Fluorescence Detectors

2.2.1 Fluorescence Detectors in the PAO

When the secondary particles of an EAS traverse the atmosphere, they interact with atmospheric nitrogen which emits fluorescence light in the wave lenght band of 300-400 nm. Fluorescence light is emitted isotropically along the trajectory of the shower and specific detectors can thus follow this trajectory and measure the energy dissipated by the particles of the shower, the air of the atmosphere being a natural calorimeter of more than 10^{10} tons. The fluorescence technique is the most efficient way to estimate the energy of the primary particle, the amount of fluorescence light emitted along the axis of the shower being proportional to the number of charged particles and allowing a direct measurement of the longitudinal development of the EAS in the atmosphere. The most important disadvantage of the fluorescence technique is its limited duty cycle of 10% as fluorescence light can only be observed during clear and moonless nights.

An air fluorescence detector, also called an "eye", consists in series of light collectors which view different regions of the sky, projecting the incoming light on specific light sensitive devices. The setup for the Pierre Auger Observatory consists of 4 stations located at the edges of the surface array (see Figure 2.1). Each eye groups 6 telescopes pointing towards different fields of view of the sky. The six telescope alignment allows a 180° cover of the sky in azimuthal angle. For each telescope, the light is reflected on a spherical mirror onto a camera of 440 hexagonal PMTs.

A precise calibration of the fluorescence detectors is essential to achieve precise estimations of the shower energy. At the PAO, uncertainties of less than 15% in the reconstructed energy can in principle be achieved. An absolute calibration of the FDs is made 4 times a year using specific sources of light [22]. Many relative calibrations are performed before, after and during data taking in order to control constantly the conditions appropriate for FD measurements.

2.2.2 Shower Parameters Reconstruction with FD Measurements

When a FD detects a cosmic ray cascade, it sees a spot of ultraviolet light moving rapidly in a circle path across the night sky. At the detection level, this is reproduced by a time sequence of light recorded by the photomultipliers making up the camera device, this sequence often spreading over two

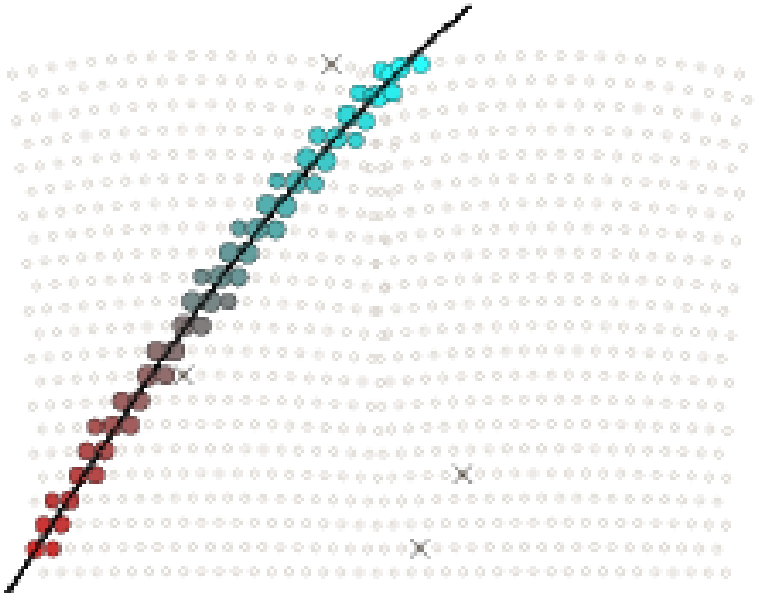

Figure 2.5: *Example of a sequence of triggered pixels of a fluorescence detecting device. The color code indicates the temporal order (blue to red).*

or more telescopes of an eye. An example of FD measurement is shown in Figure 2.5. Each grey dot corresponds to a pixel (one of the 440 PMs of the camera). The color code applied to the pixels defines the temporal order in which the pixels were triggered by the light emitted from the shower.

The first stage in finding the trajectory of a shower consists in determining the *shower-detector plane* (SDP). This is done using a fit to the eye's hit tube directions, where each point is weighted by the recorded amplitude of the light signals. The plane normal vector used to construct the SDP can be at present estimated with an accuracy of 0.2°. The geometry of a shower as seen by an eye is shown in Figure 2.6. As can be seen, the SDP is described in terms of three parameters and the arrival time of light from the shower at each triggered pixel (PMT) in the camera can be expressed as:

$$t_i = T_0 + \frac{R_p}{c} \tan\left(\frac{\chi_0 - \chi_i}{2}\right) \tag{2.2}$$

R_p is the impact parameter for the intersection of the shower with the detector. χ_0 is the orientation angle of the shower in the SDP and χ_i is the ith PMT's elevation angle in the SDP[2]. Finally, T_0 is the time at which the

[2]The speed of light is of course denoted by c.

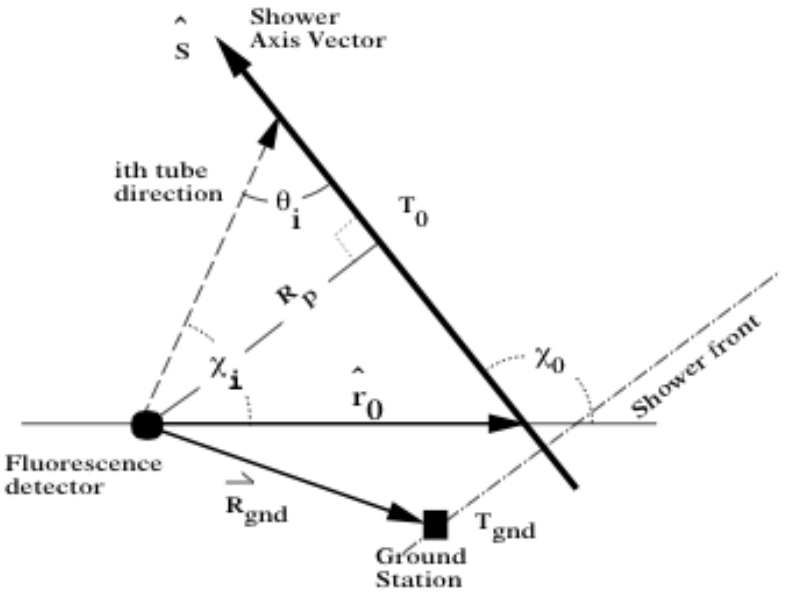

Figure 2.6: *Geometry of an extensive air shower a seen by a fluorescence detector.*

shower front is closest to the eye (i.e. at a distance R_p of the detector). The shower parameters can then be found using a minimization procedure of the χ^2 function,

$$\chi^2 = \sum_{i=1}^{N} \frac{(t_i - t_{obs,i})^2}{\sigma_i^2} \tag{2.3}$$

where $t_{obs,i}$ is the observed trigger time and σ_i the estimated uncertainty on the measurement of t_i. The minimization procedure can be difficult depending on the type of sequences recorded. For monocular detection (only one eye FD detected shower), the resolutions achieved are of the order of 1° and 600m for the arrival direction and the core position respectively. Using two eyes for the fluorescence measurements, the resolution on the arrival direction estimation can be improved up to 100m. However, one of the interest of the hybrid nature of the PAO is that the same accuracy can be achieved using the timing information of a single SD station combined to a unique FD measurement.

Once the geometry of a shower is determined, the shower energy estimation is almost straightforward. As already mentioned, the light signal registered in a pixel is not constant but through each individual PMT, the

signal rises, levels off and falls again. This information is used to obtain a relation of the fluorescence light generated by the shower particles as a function of atmospheric depth. Such reconstructions of shower profiles require the use of complex models to correct from any background effects: starlight, atmospheric airglow, man-made light pollution and also the C̃erenkov contributions from the shower particles. A model describing the relation between the light scattered at the detection level and the light produced at the shower front must also be taken into account. The obtained longitudinal profiles are then used to estimate the total energy of the shower by integrating the function describing the profiles over the atmospheric depth traversed by the shower. In fact, the fluorescence light emitted by the shower particles is proportional to the energy deposited in the volume (here the atmosphere as a calorimeter), itself proportional to the number of charged particles in the medium. A final correction using simulations for the energy carried out by neutrinos and high energy muons is applied.

2.3 Detection in Hybrid Mode

Not only because it is the largest detector ever build, the PAO is also unique because it offers for the first time two independent ways of detecting a cosmic ray. We have seen these two conjoined techniques are the typical surface array arrangement and the fluorescence detection. With these two methods, the PAO offers the possibility of obtaining very precise calibrations using the reconstructed parameters, obtained simultaneously with both techniques, for a small number of showers seen by both devices. In the hybrid mode, the Pierre Auger Observatory can achieve, in principle, a 6% energy resolution and an angular precision of 0.5° at 10^{20}eV. The uncertainty on the energy estimation remains at present of the order of 22%.

Chapter 3

Properties of Extensive Air Showers

From Chapter 1, it is evident that the mass composition of UHECRs is a key towards understanding the origins of these particles. Measuring the composition of cosmic rays is however a very difficult challenge as one must infer the nature of the primary particles from the billions of secondary particles produced in the shower. The determination of mass for UHECRs is thus always indirect and must exploit features of the development of EAS correlated to the mass of the primary. In this chapter we describe the main properties of the development of EAS in the atmosphere that can be used to estimate mass composition of primaries. The relation with the measured experimental parameters is rather indirect and must be correlated to the EAS properties. We do not give here a complete description of EAS but rather the essential material needed for the understanding of this work.

3.1 The Longitudinal Development of Extensive Air Showers and the X_{max} Parameter

The main observable describing the longitudinal development of EAS is the *depth of shower maximum*, X_{max}, defined as the atmospheric depth at which the number of charged particles in a shower reaches a maximum.. The atmospheric depth is a distance measured from the top of the atmosphere in units of g.cm^{-2} [1]. For a given energy, showers are more penetrating (larger X_{max}) for photon primaries than protons or more heavy particles. As the energy of

[1]The number of interactions a cosmic ray undergoes while it's journey to earth is proportional to the density, in g.cm^{-3}, times the path length, in cm.

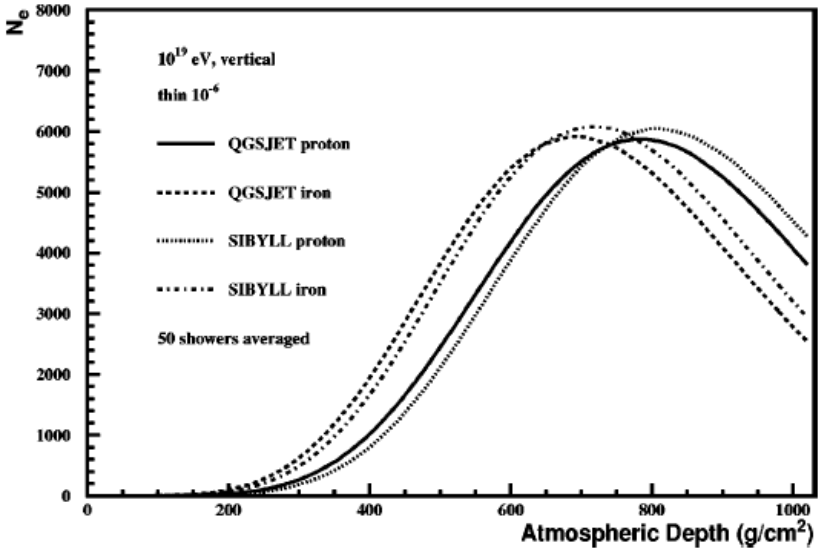

Figure 3.1: *Average development of a EAS of* $10^{19}\,eV$ *for different primaries and using different Monte Carlo simulations. The vertical axis* N_e *is the total number of electrons. Each curve results from an average of 50 proton and iron simulated showers.*

the primary increases, showers also penetrate deeper in the atmosphere and produce larger values of X_{max}.

An example is given in Figure 3.1, taken from [1]. We see that even considering different interaction models in the simulations, the position of X_{max} is different for proton and iron primaries, with a difference of about $90 \sim 100$ g.cm^{-2}. The fact different interaction models don't give the same predictions is a source of systematic uncertainties inherent to mass composition studies. Here the discrepancy between the models is of the order of 25 g.cm^{-2} which means the disentanglement between the two species is still possible.

The correlation of the X_{max} parameter with the mass composition of the primary specy can be explained using the simplified Heitler model, describing the development in the atmosphere of EAS. First we use the model to describe electromagnetic showers and then we apply the same arguments to the case of hadronic showers.

3.1.1 X_{max} for Electromagnetic Showers

Photonic showers induce photon and electrons as secondaries via radiative process. Photon undergo pair-production while electrons loose energy via Bremsstrahlung. For pair production, the photon gives birth to an electron-

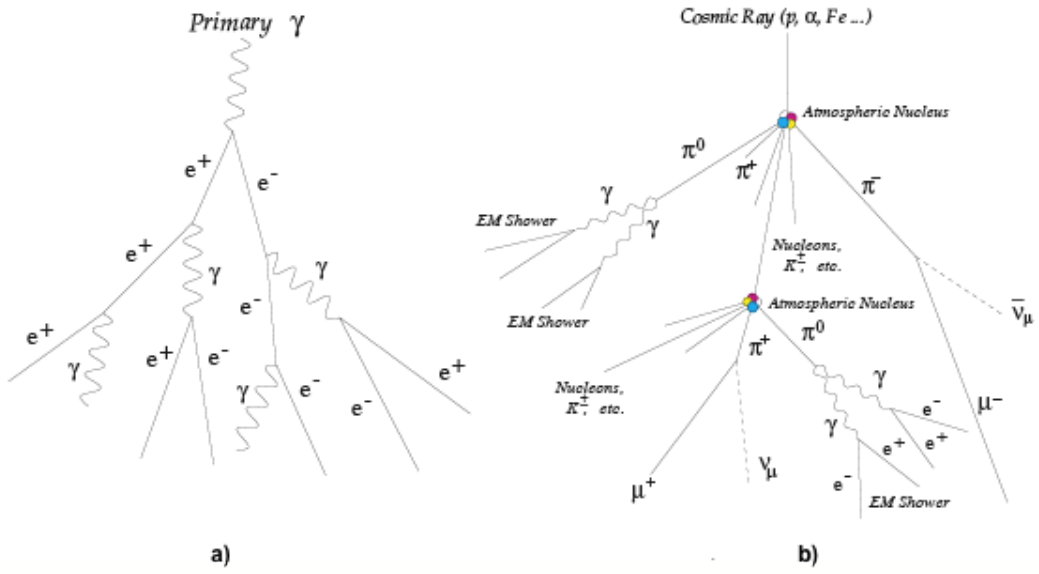

Figure 3.2: *Schematic picture of the development of EAS using the simple arguments of the Heitler model for (a) electromagnetic showers and (b) hadronic showers. Picture taken from [18].*

positron pair. It is assumed that after a spread distance d, a photon is emitted through a Bremsstrahlung process, taking half of the energy of the parent electron. Figure 3.2 (a) illustrates the development of an electromagnetic shower using these simple arguments. The average splitting length d is related to the radiation length of the electron, λ_r, by:

$$d = \lambda_r \ln(2) \qquad [g.cm^{-2}] \tag{3.1}$$

The actual probability that a photon of a given energy is emitted via Bremsstrahlung is inversely proportional to the photon's energy and d is the average length for which half of the energy of the electron is converted in photons via a radiative process. For simplicity, we keep the assumption of the equal energy distribution between an electron and a photon after a distance d.

The pair-production cross-section is related to the one for Bremsstrahlung from electrons by a simple formula:

$$\sigma_{pair} = \frac{7}{9}\sigma_{brem} \tag{3.2}$$

Considering the similarity between these two cross-sections, we assume photons undergo pair-production after the same splitting length d. Thus,

after n splitting length, the number of particles in a electromagnetic shower is 2^n and their energy is given by $E/2^n$ where E is the energy of the primary photon.

The number of particles in the shower continues growing until they reach a critical energy, ϵ_c, for which the loss rate of energy due to radiative processes becomes lower than the one from ionization. At this point the shower reaches a maximum and the number of particles in the shower starts to decrease with the remaining particles still dissipating energy by ionization in the atmosphere. The particles produced at each step share the energy of the parent equally. We have for the particles at shower maximum, $N_{max} = E/\epsilon_c$, and for the depth of maximum, $X_{max} = nd = \lambda_r \ln(N_{max})$. Combining both equations and getting rid of N_{max}, we obtain:

$$X_{max} = 2.3\lambda_r \log_{10}(\frac{E}{\epsilon_c}) \qquad [g.cm^{-2}] \tag{3.3}$$

The simplifications used here do lead to some uncertainties: the N_{max} number predicted by the model is larger than the one measured in experimental data. This is explained by the fact the model neglects the attenuation lengths of photons and electrons. The production of multiple photons in the Bremsstrahlung also affects the value of N_{max}. However, the model remains appropriate for describing the development of showers in terms of X_{max}.

3.1.2 X_{max} for Hadronic Showers

The Heitler model can also be used to describe the longitudinal development of hadronic showers. The main difference lies in the description of the firsts interactions of the cosmic ray with the atmosphere. Considering for instance a proton primary with energy E and an interaction length λ_I, the first interaction of the proton with an nucleus of the atmosphere takes place after a distance $X_0 = \lambda_I \ln 2$. This inelastic process creates a certain number of pions, denoted N_π and known as the multiplicity of pion production. The fraction of energy of the primary used in the formation of the shower is called the inelasticity parameter, denoted κ. The energy directed into a shower through the pion production process is therefore κE. The variables N_π and κ are both poorly known at the highest energies and need to be extrapolated from our knowledge at lower energy. As thus, they are the main source of systematic uncertainties in the simulation of extensive air showers and hence on the mass estimations. Future results from the LHC should however constraint these parameters at a higher level of accuracy.

In the first interactions with the atmosphere, the proton produces a variety of hadrons (protons, neutrons, kaons, pions, etc.). The main contribution is the one of pions. The proton produces a neutral combination of pions. This means a $\pi^0 : \pi^+ : \pi^-$ ratio of $1 : 1 : 1$. Pions then initiate other hadronic sub-showers or decay into muons. This is illustrated in Figure 3.2 (b). The sub-showers are neglected in our simplified model. We are left with charged pions decaying into muons and neutral pions forming pair of photons, thus initiating electromagnetic showers. π_0 being $1/3$ of the pion production ratio, each photon will then initiate a shower of energy $\kappa E/(6N_\pi)$. Inserting this in equation 3.3, we obtain:

$$X_{max} = X_0 + 2.3\lambda_r \log_{10}\left(\frac{\kappa E}{6N_\pi \epsilon_c}\right) \qquad [g\ cm^{-2}] \tag{3.4}$$

For the case of heaver nuclei, we consider a superposition model which essentially states that for a nucleus of energy E and atomic mass A, each nucleon shares equally the energy of the nuclei and initiates independent showers developing along each others. This means we can use the same arguments as for proton initiated showers with each proton having a energy of E/A. Using equation 3.4, we have:

$$X_{max} = X_0 + 2.3\lambda_r \log_{10}\left(\frac{\kappa E}{6AN_\pi \epsilon_c}\right) \qquad [g\ cm^{-2}] \tag{3.5}$$

Equations 3.4 and 3.5 describe longitudinal profiles from which the X_{max} values obtained agree well with the more complex simulations used in Figure 3.1. As already mentioned, we find that high energy protons penetrate deeper in the atmosphere and thus produce larger values of X_{max}. A fact that cannot be accounted by the Heitler model is that the interaction length of a nuclei decreases with the atomic mass A and thus the first interactions with the atmosphere appear at smaller atmospheric depths. Therefore, showers initiated by heavier nuclei develop faster in the atmosphere and the shower maximum is reached sooner.

3.1.3 The Elongation Rate

The average rate of change of X_{max} as a function of energy is called the *elongation rate*, D_e. This concept was first introduced by John Linsley [23] who demonstrated that D_e could be used as a measure of the rate of change of composition with energy. If the mass composition of cosmic rays was to be constant over a certain range of energies, then we can expect a constant value

of the elongation rate. Reciprocally, measuring changes in the elongation rate is an indication of changes in the mass spectrum of cosmic rays. One usually considers the rate of change per decade D_{10},

$$D_{10} = \frac{\partial X_{max}}{\partial log_{10} E} \quad [g.cm^{-2}/dec]. \tag{3.6}$$

From equation 3.3, we have for electromagnetic showers:

$$D_{10} = \frac{\partial X_{max}}{\partial log_{10} E} = 2.3\lambda_r \quad [g.cm^{-2}/dec] \tag{3.7}$$

This expression of D_{10} gives a good description of the change in X_{max} when compared to more complex analysis. The radiation length of electrons in the air is of 37 g.cm^{-2} and the critical energy is 85 MeV. the Heitler model then predicts an increase in X_{max} of 85 g.cm^{-2} per decade of energy for electromagnetic showers, a value close to the one obtain with simulations.

For the hadronic case, our lack of knowledge in the pion multiplicity N_π and inelasticity constant κ of the first interactions leads to less accurate estimations. However, an good estimation is given by:

$$D_{10} \sim \frac{\partial}{\partial \log_{10} E}\left(2.3\lambda_r \log_{10}\left(\frac{E}{A\epsilon_c}\right)\right) - 27\ g.cm^{-2} \tag{3.8}$$

This expression gives an elongation rate for hadronic nuclei of $D_{10} \sim$ 58g.cm^{-2}.

The relation of the elongation rate to mass composition is clear when considering an example. Figure 3.3 presents results from hybrid data measured at the Pierre Auger Observatory (black dots). The red and blue lines are the simulated elongation rates for proton and iron primaries respectively, using different interaction models. It appears from these results that a change in composition of cosmic rays is observed at an energy of 2×10^{18} eV, which coincides with the ankle feature of the energy spectrum of cosmic rays (see section 1.1). Over this energy, a heavier composition of cosmic rays is suggested by the data. However, we must again stress the fact that such a conclusion and a precise estimation of the composition depends strongly on the interaction model used. These methods expect a lot from the future results from accelerator experiments to reduce the discrepancies between the different model predictions.

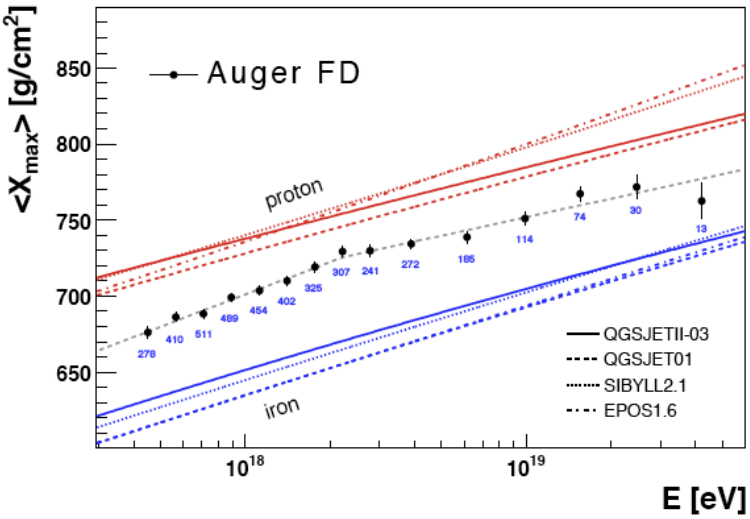

Figure 3.3: *Example of the simulated elongation rates for proton and iron primaries (red and blue lines respectively). The black dots represent data from hybrid events measured at the Pierre Auger Observatory. A change in the mass composition of cosmic rays is observed around* 2×10^{18} *eV. The picture is taken from [18].*

3.1.4 The Fluctuations in X_{max}

From the discussion of the previous sections, we understood that the depth of maximum of a shower, X_{max}, is correlated with the mass of the primary particle initiating the shower. The development of a shower is a statistical process and the position of X_{max} for the same primary fluctuates from a shower to another. Also, these fluctuations in X_{max}, $\sigma_{X_{max}}$, can be correlated to the mass of the primary. This can be understood by the fact that for heavy nuclei (heavier than proton), each nucleon initiates independently his own sub-shower using a part of the energy of the parent particle, equally spread with the other nucleons. This reduces the Poisson fluctuations in the development of the shower and thus in X_{max}. In a more accurate model, it must be taken into account that not all nucleons actually initiate sub-showers in the first interactions. The original nuclei usually disintegrates in several fragments inducing further sub-showers. Again, this reduces the fluctuations in the later development of the shower compared to a proton shower. In conclusion, showers initiated by heavier particles fluctuate less in their development than proton initiated showers. In other terms, measuring the fluctuations in the X_{max} parameter, $\sigma_{X_{max}}$, offers a possibility of making mass composition measurements. Typically, the measured $\sigma_{X_{max}}$ are plotted

as a function of energy. Sudden changes in $\sigma_{X_{max}}$ are then indicative of mass changes in the cosmic ray flux at the different energies (in the same manner it is done for the elongation rate, see previous section).

3.2 Mass Composition Measurements

A great advantage of the fluorescence detection technique is the fact it allows to measure directly X_{max} on a shower-by-shower basis. The resulting X_{max} distributions can then be used to extract information on the primary species by comparison with simulations, using the elongation rate discussed in the previous section. However, we have seen that the duty cycle of the FDs is limited (10%) and a technique using the detectors of the surface array is desirable. This is done finding new observables that can be correlated to the depth of shower maximum and thus to the primary composition. The principal measurement for this, using surface detectors, is the arrival time distributions of the shower particles. We also mention the interest of the ratio of muon to electrons as a mass correlated parameter. Other techniques exist but have not yet been proven entirely successful. Among others, there is the lateral distribution of particles, the radius of curvature of the shower front or the Zatsepin-Gerisamova effect, using the photo-disintegration of heavy nuclei in the radiation field of the sun. We do not discuss these methods here. Reference [18] gives a short overview.

3.2.1 Shower Components at Ground and the Muon to Electromagnetic Ratio

An array of particle detectors such as the one of the Auger Observatory is sensitive to the lateral distribution of particles. Considering hadronic interacting showers, the principal components at the detection level are photons, electrons and muons[2]. For proton and iron primaries, the density of photons and electrons is almost identical over a wide region of distances from the core and cannot be used to distinguish the two primaries. Even though iron cascades develop higher in the atmosphere and should therefore induce particles spread more broadly at ground, the particles also have to travel greater distances compared to proton showers and the fact there is more attenuation for these particles explains why the two effects compensate at the end. Of course, electromagnetic gamma-ray showers show very distinctive properties

[2]A very small contribution of hadrons is found close to the shower core but is rapidly negligible at distances larger than 100m

as they penetrate much deeper in the atmosphere and induce steeper lateral distributions with very fewer number of muons.

As for muons, their densities are different for proton and iron primaries, not by a large amount but enough to distinguish them by precise measurements. On average, iron showers produce 1.45 times more muons than proton ones [24]. This is because showers initiated by heavier nuclei are composed of sub-showers initiated by the nucleons which share equally the energy of the primary [3]. The energy of the pions produced in the early stages of the development is therefore reduced compared to a proton shower of the same energy. This implies that more muons are produced. As the number of electrons remains the same, we can expect the muon to electromagnetic ratio to increase with the atomic number. The ratio for the number of muons to the number of electrons can thus be used as a mass estimator. This was done and proved successful for the first time in the KASCADE experiment [4]. However, the ratio is difficult to determine precisely with the surface detectors of the Auger Observatory. In fact, with the C̃erenkov detection technique employed, the two muon and electromagnetic components cannot be easily separated. Alternative methods using the ratio of interest have however been developed and used with success. The main difficulty then remains the use of interaction models for the simulations of the electromagnetic and muon component at the detection level. These predictions always suffer the inherent uncertainties coming from the choice of the interaction model (essentially pion multiplicity N_π). Such a method has been the object of this work and will be described in all details in Chapter 4.

3.2.2 Arrival Time Distributions of Shower Particles

The time structure of shower particles arriving at ground can be used to extract information on the longitudinal profile of the shower an thus on X_{max}. This can be understood using some simple geometrical arguments. In Figure 3.4 are drawn two showers of the same inclination (same angle θ) but with different depths of maximum X_{max}, (b) showing a shower penetrating deeper in the atmosphere than (a). The path lengths differences between the distances d_3 and d_4 are smaller than for the distances p_3 and p_4 (i.e. for the two distances d_1 and d_2 compared to p_1 and p_2). This means the path lengths differences travelled by particles emitted in the early and late part of the shower increase with X_{max} and the spread in arrival time is greater for deeper showers. The time distribution of particles is therefore correlated

[3] This is the case in the simple *superposition model* we have considered until now, see section 3.1.2

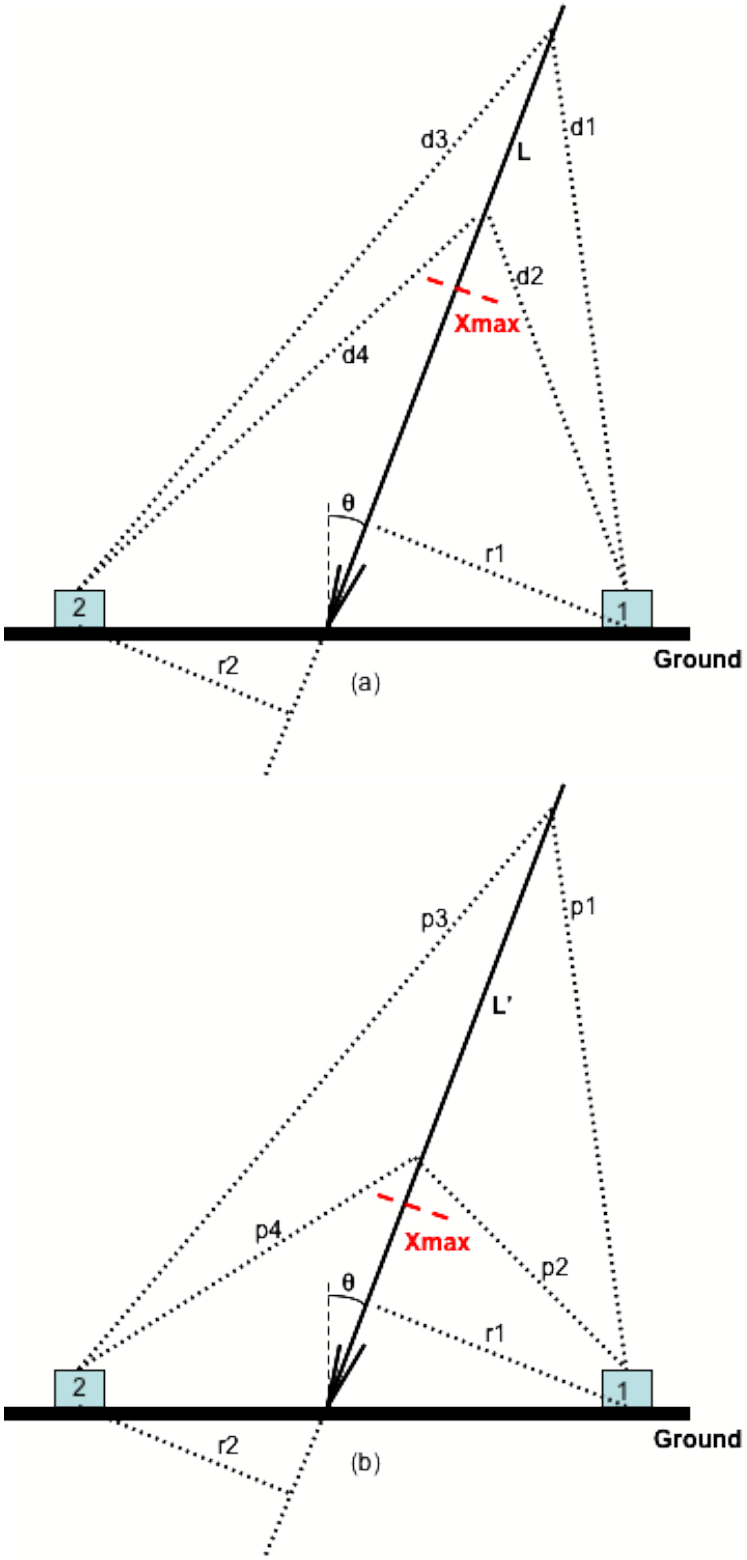

Figure 3.4: *Geometrical representation of two extensive air showers with the same inclination but different X_{max}. (a) shows a shower developing earlier in the atmosphere than (b). This example can hold for a iron primary, (a), and a proton, (b).*

to X_{max} and thus to the primary composition. Further, the path lengths differences also increase with the distance to the core r and the spread in arrival time therefore increases with r, from a geometrical point of view[4]. With increasing values of the zenith angles, it is clear the effect also grows as the differences in path lengths increase. The temporal spread in particles is also affected by velocity differences of the particles, Coulomb scattering and deflections in the magnetic field. These effects typically induce a increased broadening of the spread in arrival times. For zenith angles under 60°, the geometrical effect was shown [25] to dominate.

When measuring the spread in arrival times of shower particles in a station, no difference is made between the type of particles detected. Also, the features of the temporal distributions cannot be understood without considering the fact that muons and electrons, for instance, are not affected in the same way by the effects mentioned above. In [26], it was observed that the time spreads at large core distances were greater than what was expected from the simple geometrical arguments. This was explained by the fact that electronic component is delayed by scattering processes while the muonic component basically travels through the atmosphere without interacting. This effect can easily be understood to increase with the distance to the core as larger distances must be travelled by the particles. The temporal distributions are therefore further spread in time. However, one must observe that the electromagnetic component also undergoes absorption and for very inclined showers with small X_{max}, far from the core, the electromagnetic component almost completely disappears. The detected signal is therefore dominated by the muons which arrive faster and less delayed in time. The resulting time distributions are then much less spread in time.

Finally, we must mention a last effect observed in the time distributions. For a vertical shower, we expect the spread in the distributions to be the same for stations at the same distance from the core. However, for inclined showers, an asymmetry appears as the atmospheric depths traversed by the particles are different depending on the position of the stations around the core. This asymmetry shows features of great importance as it can be related to the mass of the primary cosmic ray. A method exploiting this asymmetry for mass composition studies is described in Chapter 4, as the basis of this work.

[4]It is important to know that the relation of the risetime with the distance to the core is linear only over a certain range of distances to the core, typically from 400m to 2000m.

3.2.3 The RiseTime Parameter $t_{1/2}$

The signals recorded by the surface detectors of the PAO are a convolution of the effects of the different shower particles traversing the tanks and some inherent detector effects (see section 5.1.1). The spread in arrival times of shower particles are measured by evaluating a fixed segment of the total integrated signal for each station. Historically, the first parameter defined was the *risetime*, $t_{1/2}$, the time it takes the signal to rise from 10% to 50% of the total integrated signal. The reason for this choice was related to the experimental resolutions that could be achieved at the time. The first part of the signal is used because it contains particles created in the early stages of the shower and that can be related more precisely to their production distance compared to late particles, essentially electrons, highly affected by the interaction with the atmosphere. Even though there is no *a priori* reason for this parameterization to be the one that describes the most accurately the development of a shower, several studies have been made using other parameterization of the risetime and no improvement of the correlation with X_{max} was obtained [5]. The risetime parameter was first shown to be a mass sensitive parameter in [27] where the large fluctuations observed between different showers could not be explained only by the sampling uncertainties. Simulations then showed that the risetime parameter could be correlated to X_{max}. Although a direct measurement of X_{max} cannot be made by surface detectors, the hybrid nature of the PAO allows for a direct calibration between the measured risetimes and X_{max} in a small sample of "hybrid" events. This calibration can then be used to infer X_{max} for the larger set of SD data.

3.2.4 Deviations in the Risetime Parameter

As can be expected, as the fluctuations in X_{max} are sensitive to the primary mass, the fluctuations in the measured risetime parameter $t_{1/2}$ can also be correlated to the primary composition. This was done in [27] where the observed fluctuations in $t_{1/2}$ could not be explained only by measurements uncertainties but were further shown, through simulations, to be induced by the natural fluctuations in the shower development (see section 3.1.4).

A method using the fluctuations in the risetime parameter was developed in University of Leeds by the group of Alan Watson. We briefly summarize the technique that is used. For more information, see reference [18].

[5] See for example [18]. At present, other tests with a risetime parameter defined from 10% to 30% of the integrated signal are currently under study in University of La Plata.

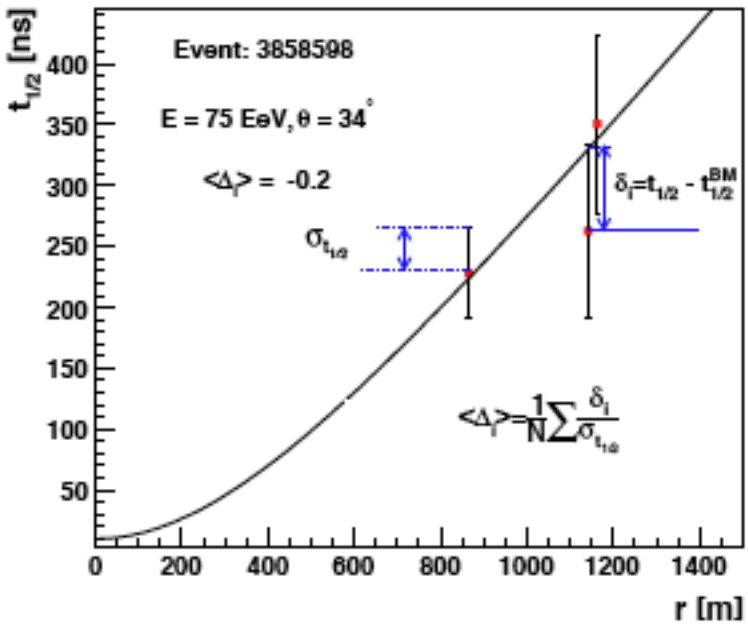

Figure 3.5: *Schematic representation of the method used to calculate the* $\langle \Delta_i \rangle$ *parameter.* δ_i *is the deviation of the risetime value from the one predicted by the benchmark function (black line).* $\sigma_{t_{1/2}}$ *are the uncertainties on the measurements of the risetime from the detected signals. The picture is taken from [18].*

When a shower hits the surface array, several signals are detected for the event and thus several measurements of the risetime can be made. In order to use this information on an event-by-event basis, it is more appropriate to associate a single parameter to these individual measurements. A new parameter is therefore introduced which can be defined with one or more measurements of the risetime in a shower. Of course this parameter must exhibit the appropriate dependencies of the risetime with the core distance and the arrival direction which we know to be related to the depth of shower maximum and thus to primary composition. Finally, the parameter must be dependent on X_{max} in hybrid events in order to be calibrated and further to allow a calibration for SD only events.

The method consists first in defining a fit to the average measured $t_{1/2}$ as a function of core distance for showers at a fixed energy, in order that the average X_{max} is also fixed for these events. The new parameter introduced is $\langle \Delta_i \rangle$ which is the average deviation of the risetimes measured in each station in an event from those of the benchmark function fit. For each

signal, this average deviation is calculated in terms of the uncertainty in the measurement of the risetime, $\sigma_{t_{1/2}}(S, r, \theta)$:

$$\Delta_i = \frac{t_{1/2} - t_{1/2}^{BM}(r, \theta}{\sigma_{t_{1/2}}(S, r, \theta)} = \frac{\delta_i}{\sigma_{t_{1/2}}(S, r, \theta)} \tag{3.9}$$

For N signals recorded from a shower, we can then combine the individual deviations in a single parameter characteristic of each event,

$$\langle \Delta_i \rangle = \frac{\sum_{i=1}^{N} \Delta_i}{N} \tag{3.10}$$

As we know the average risetimes of signals increases with X_{max}, the average deviations from the benchmark function should also increase with X_{max} and therefore $\langle \Delta_i \rangle$ reflects the position of X_{max}. Figure 3.5 presents a schema of how the $\langle \Delta_i \rangle$ parameter is calculated.

The technique described here is very sensitive to the accuracy with which the risetime values can be obtained. Also, the events selected for the analysis obey very tight selection criteria on the distance from the core and the arrival direction of the detected showers. The justifications for all these selections are describes in [18], Chapter 4. Further, in order to achieve the best results, the authors suggested a deconvolution procedure to correct the signals from any detector effects. This procedure was intensively studied and showed to introduce strong differences between the de-convoluted and convoluted risetimes. Furthermore, the associated uncertainties were improved with the procedure and this previous treatment appeared indispensable for the method. The question wether the corrections applied in this technique should be further extended to other methods where the risetime is used as the relevant experimental parameter has motivated this work. We address this question in the following chapters.

Chapter 4

Mass Composition Estimation from the Time Distribution Asymmetry

In Chapter 1, we have stressed the importance of studying the mass composition of UHECRs. As mentioned above, our knowledge on composition at energies above 10^{18} eV is very poor and a method for investigating this unknown is essential. In this chapter we discuss in detail the method using the features of the asymmetry observed in the rise time parameter $t_{1/2}$ as a surrogate for mass composition.

4.1 Asymmetries in the Arrival Time Distributions of Particles

In ground array experiments, events are traditionally reconstructed assuming the observation depends only on the perpendicular distance to the axis of the shower[1]. This assumption is not verified for inclined showers. If one considers the shower plane, the plane perpendicular to the axis of the shower (see Figure 4.1), on which the signals registered by the detectors are projected, two additional effects have to be taken into account compared to vertical showers:

- A geometric effect due to the inclination of the shower combined to the fact the particles of the shower hit the detectors at different angles, which affects mainly showers with inclinations lower than 30°;

[1]At present, technics start to be developed and used for correcting parameters from different effects before projecting them on the shower plane.

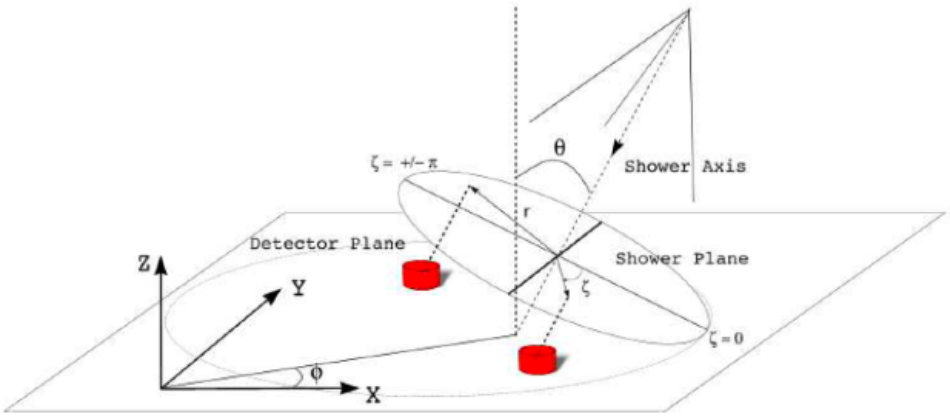

Figure 4.1: *Schematic view of the shower geometry. In the shower plane, the "early" region corresponds to* $\zeta \in [0, \pm\pi/2)$ *and the "late" region to* $\zeta \in [\pm\pi/2, \pm\pi)$*. The different amount of atmosphere traversed by the particles of these to region before reaching the detectors is clear.*

- An effect of atmospheric absorption of the electromagnetic component of the shower, which is different for particles around the core of the shower as they go through different amount of atmosphere. This effect dominates for showers with inclinations above 30°;

These effects result in an asymmetry in the arrival time distributions of particles, as can be seen in Figure 4.2 which gives a schematic view of showers with the same position of shower maximum X_{max} but arriving on earth with different inclinations, i.e. different zenith angles θ. In the case of a vertical shower, particles traverse the same amount of atmosphere before reaching the detectors and therefore no azimuthal asymmetry appears. At a given distance from the core, the ratio of the muonic to electromagnetic component is constant. Going to inclined showers, distances travelled by the particles arriving in the early ($\zeta \in [0, \pm\pi/2)$) and late region ($\zeta \in [\pm\pi, \pm\pi/2)$) of the shower plane are different, and therefore, the electromagnetic component suffers more absorption in the atmosphere for late particles. As for muons, they do not suffer from any absorption and arrive earlier and over a shorter period of time. Therefore they dominate the first portion of the signal in the SD stations. In terms of measured rise times, larger values are found in the early region, with a stronger influence of the electromagnetic part. This results in an asymmetry with azimuthal angle ζ of the time distribution of particles. This characteristic behavior is well illustrated in Figure 4.3. The

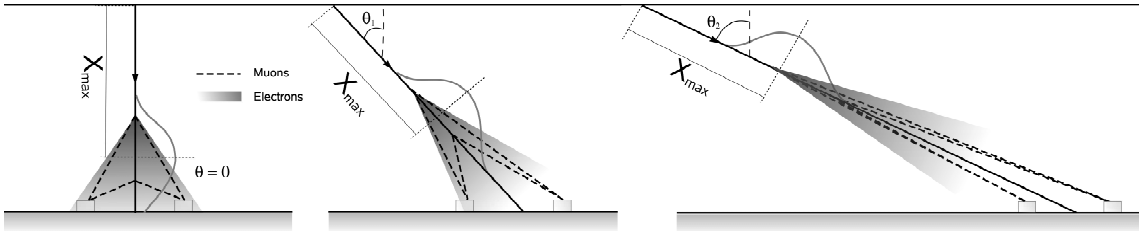

Figure 4.2: *Showers with the same X_{max} entenring the atmosphere at different zenith angles. The increasing differences of depth of atmosphere traversesd by particles in the "early" and "late" regions are clear. The parameters a and b used to describe the asymmetry are shown and described later in the text.*

plots corresponds to a real set of data selected for certain bin of energy, $18.5 < \log[E(eV)] < 19.0$, and zenith angle, $36° < \theta < 42°$, as calculated at the Pierre Auger Observatory.

However, as showers become even more inclined, the amount of atmosphere traversed by the particles increases and at some point the electromagnetic component is almost completely absorbed, leaving the muonic component, basically free of asymmetry, alone at ground. In other words, the asymmetry increases with zenith angle and is expected to reach a maximum before decreasing again for higher inclinations. This is shown in the left plot of Figure 4.4 were we have plotted the azimuthal time distributions of showers of the same energy but arriving at different zenith angles.

We have shown that time distributions of signals recorded by surface detectors contain implicit information on the shower development. Recalling the definition of the rise time parameter $t_{1/2}$ as the time to reach from 10% to 50% of the total integrated signal in each station (see section 3.2.3), the azimuthal asymmetry further applies to this time parameter and depends on the atmospheric depths traversed by the particles in the shower, and therefore depends on both the depth of shower maximum and zenith angle. These dependencies explain the sensitivity of timing parameters to mass composition since the shower development is, for instance, not the same for proton and iron primaries. The procedure to extract the values of the asymmetry is explained in the next section.

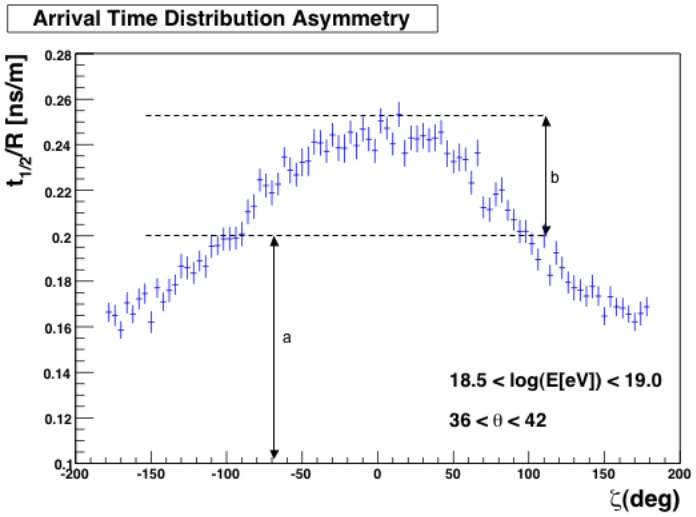

Figure 4.3: *Illustration of the asymmetry with azimuthal angle of the arrival time distribution of particles in the detector. Errors bars come from statistical uncertainties when averaging values of rise times in bins of* ζ*. The parameters* a *and* b *are the ones from equation 4.7.*

4.2 Asymmetry Parameters

To extract values of asymmetries from the azimuthal profiles of the risetime, we need to use a parameterization of the characteristic behavior of the risetime with azimuthal angle (Figure 4.3). This can be done considering some simple arguments. It has been shown that the *slant depth*[2] of particles in the shower, t', can be expressed using a Taylor expansion around $t_s = t \sec\theta$, where t is the vertical atmospheric depth at ground. Since the azimuthal angle correction is small compared to the total slant depth, in a first approximation one can keep only the first term which is equivalent to using a linear function in $\cos\zeta$ to describe the asymmetries ([28]). Formally, the parameterization is described as follows.

$$t'(\zeta) = t \sec\theta(1 + B\cos\zeta) = t_s + \Delta t_s(\zeta) \tag{4.1}$$

If $\tau(r,t)$ represents the time distribution of particles for a vertical shower,

[2]The "slant depth" is essentially a generalization of the 'interaction depth". The latter, in units of $g.cm^{-2}$, gives a measure of the path length of a particle that helps predict the absorption it undergoes. However, the standard calculations of the interaction depth only holds for particles arriving vertically and the slant depth is used to extrapolate an equivalent altitude that would correspond with this depth if it were vertical.

then, for inclined showers, we have the correction:

$$\tau(r,t) \longrightarrow \tau(r,t'(\zeta,\theta)) \tag{4.2}$$

where r is measured in the shower plane. A Taylor expansion of τ around t_s gives:

$$\tau(r,\zeta) = \tau(r,t'(\zeta)) = \tau(r,t_s + \Delta t_s(\zeta)) \tag{4.3}$$

$$\tau(r,\zeta) = \tau(r,t_s) + \frac{\partial\tau}{\partial t'}|_{t_s}\Delta t_s(\zeta) + \dots \tag{4.4}$$

$$\tau(r,\zeta) = \tau(r,t_s) + \frac{\partial\tau}{\partial t'}|_{t_s} t_s B\cos\zeta + \dots \tag{4.5}$$

$$\tau(r,\zeta) = \tau(r,t_s)\Big(1 + \frac{\partial\log\tau}{\partial\log t'}|_{t_s} B\cos\zeta + \dots\Big) \tag{4.6}$$

Keeping the first term of the expansion, equation 4.6 can be expressed as:

$$\tau(r,\zeta) = a + b\cos\zeta \tag{4.7}$$

with

$$a = \tau(t, t\sec\theta) \tag{4.8}$$

$$\frac{b}{a} = B\frac{\partial\ln\tau}{\partial\ln t'}|_{t_s} \tag{4.9}$$

The asymmetry factor b/a which depends on t_s can be used as a measure of the logarithmic variation of τ with slant depth. This parameter is an indicator of the shower evolution and is therefore related to the primary composition. In other words, the dependence of the asymmetry factor with $\sec\theta$ allows us to find new observables useful for mass composition estimation.

With this parameterization, we can now obtain the different values of asymmetry. For a given bin of energy, we sample the azimuthal time distributions $t_{1/2}$ for different zenith angles and extract a value of asymmetry for each case. This allows to construct the longitudinal development of the asymmetry plotting the values of the asymmetry versus $\ln(\sec\theta)$. This is illustrated in Figure 4.4. The right plot presents the values of asymmetry extracted from the fits to the profiles presented on the left, using equation 4.7. The analysis was done using $t_{1/2}/r$ as the risetime grows linearly with the distance r to the core (see footnote page 43). As previously explained, the asymmetry reaches a maximum before decreasing for higher zenith angles. A gaussian fit to these points is expected to reproduce the behavior of the asymmetry for all zenith angles.

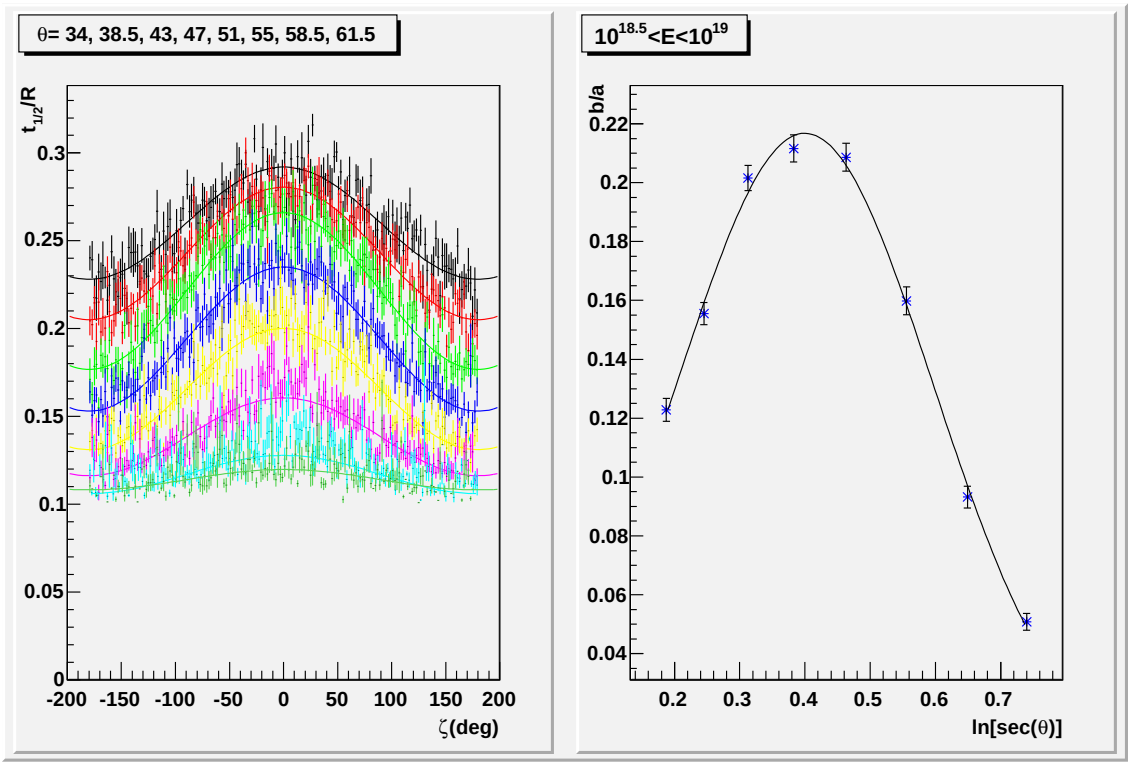

Figure 4.4: *Rise time versus azimuthal angle for different values of the zenith angle (from top to bottom,* $\theta = 34, 38.5, 43, 47, 51, 55, 58.5$ *and* $61.5°$*). We see that the amplitude of the asymmetry first increases with the zenith angle and then decreases for very inclined showers after reaching a maximum.*

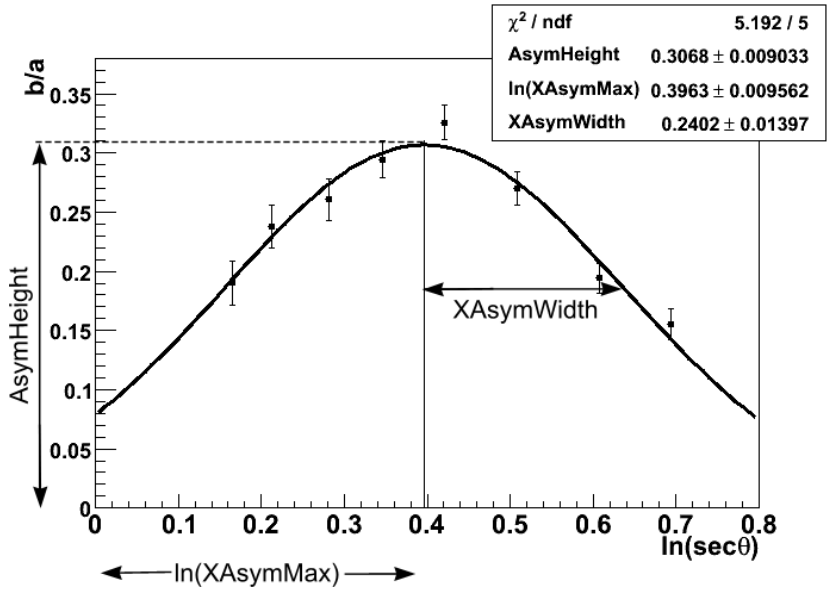

Figure 4.5: *Parameters describing the longitudinal development of the asymmetry. Three parameters are defined: XAsymMax, AsymHeight, and XAsymWidth.*

The longitudinal development of the asymmetry can be described by means of three parameters (see Figure 4.5): *XAsymMax*, the position of maximum of asymmetry, i.e. the $\sec\theta$ value for which b/a is maximum, *AsymHeight*, the height at maximum (maximum value of b/a), and *XAsymWidth*, the half width at half maximum of the Gaussian fit. Figure 4.6 gives a good illustration of the dependence of these "longitudinal profiles"[3] with primary composition. Going from a purely proton to iron composition, the profiles evolve in such a way that we can see relevant changes in the asymmetry parameters we have defined, showing therefore a clear sensitivity to primary mass. This example was obtained simulating different sets of showers reflecting different mixtures of proton and iron.

4.3 Extracting the Primary Mass

The dependence of the asymmetry parameters with primary mass has been obtained assuming a two component "proton-iron" composition. Showers

[3]We refer to the appellation "longitudinal profile" because for a given primary energy E, the asymmetry parameter b/a depends on the zenith angle θ in such a way that its behavior versus $\sec\theta$ is reminiscent of the longitudinal development of the shower.

have been simulated for these primaries changing by steps of 10% the mixture of the components, going from a pure proton composition to a composition of 100% iron. With the resulting longitudinal profiles of asymmetry, the dependence of the extracted asymmetry parameters with composition (the choice made here is the fraction of iron, x_{Fe}) can be obtained. It is observed that all three asymmetry parameters do not exhibit the same sensitivity to primary composition. For instance, looking at Figure 4.6, we see that while there is a clear dependence of *XAsymMax* and *AsymHeight* with primary composition, this is not the case for *XAsymWidth*. The same observations can be made looking at the correlation of the asymmetry parameters with the depth of shower maximum in Figure 4.7. Again no correlation is found for the *XAsymWidth* parameter. If a better understanding of the hadronic models could allow to recover a correlation even for the *XAsymWidth* parameter, then, in principle, the three asymmetry parameters could be used to maximize the information we can extract on composition [4]. Thus, considering a set of data for which composition is unknown, the iron fraction can be estimated by minimizing the function:

$$\Delta^2 = \frac{(\sigma_s - f_\sigma(x_{Fe}))^2}{\Delta\sigma_s^2 + \Delta f_\sigma^2} + \frac{(h_s - f_h(x_{Fe}))^2}{\Delta h_s^2 + \Delta f_h^2} + \frac{(m_s - f_m(x_{Fe}))^2}{\Delta m_s^2 + \Delta f_m^2} \qquad (4.10)$$

where σ, h and m stand for the asymmetry parameters, respectively *XAsymMax*, *AsymHeight* and *XAsymWidth*. The subindex s indicates the corresponding values of the sample to be studied and $\Delta\sigma$, Δh and Δm represent the standard deviations of the separation parameters. Finally, the functions $f_i(x_{fe})$ stand for the parameterization of the dependence of each parameter with the iron fraction x_{Fe}.

The sensitivity of the method to mass determination has been tested in [29] by simulating different mixtures of proton and iron (100% iron, 100% proton and a 50%-50% mixture between the two components). Deviations between reconstructed and real values of x_{Fe} are found to be less than 4%. Uncertainties of the order of 10% arise due to limited statistics in the Monte Carlo samples. Discrepancies between predictions for different hadronic models have been observed and result in differences of 15% in the obtained x_{Fe}. These remain the dominant source of systematic uncertainties. Discrepancies between values of simulated and reconstructed energies lead to an effect of less than 3%. Finally, the contribution coming from the cuts applied on the original sample has been estimated to be of the order of 3%.

[4] However, at present, this is not the case and the asymmetry analysis is performed retaining only one parameter. Later in the text we explain why the *AsymHeight* parameter is also rejected.

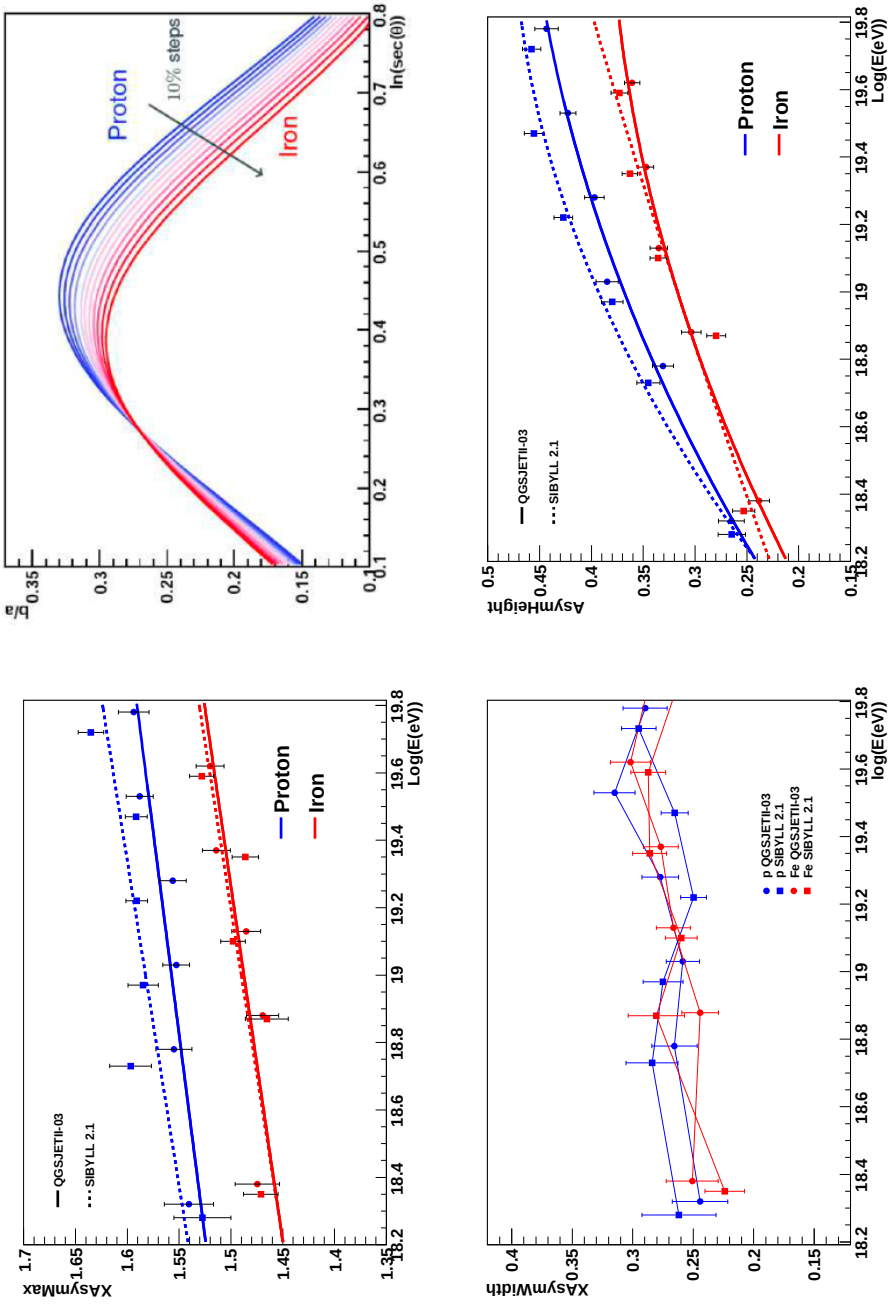

Figure 4.6: *The top-left plot shows the smooth transition in the asymmetry longitudinal profile from a purely proton to iron composition. These results where obtain using Monte Carlo models and simulating cases of different mixtures of proton and iron for an energy of* 10 *EeV. The three other figures show the asymmetry parameters dependencies with energy for QGSJETII(03) and SIBYLL 2.1.* (figure taken form ref. [29])

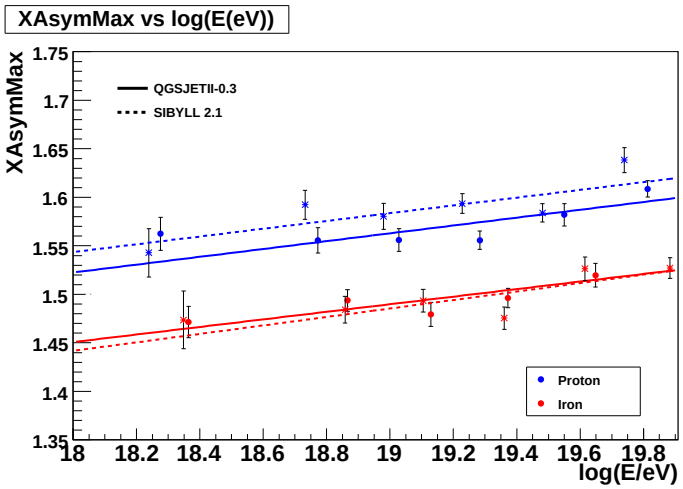

Figure 4.7: *XAsymMax vs. Energy. The results for two different models are potted, QGSJETT(03) in solid lines, SIBYLL 2.1 in dashed lines. Proton results are in blue, iron in red.*

A clear picture of the way the method works can be obtained by plotting the asymmetry parameter *XAsymMax* versus *Energy*. Such plots show strong analogy with the well-known elongation rate (the logarithmic rate of change of the depth of shower maximum with energy, $dX_{max}/d\ln E$). In Figure 4.7, we simulated using the method previously described the behavior of *XAsymMax* with energy for a 100% iron composition (red lines) and a 100% proton composition (blue lines). Solid and dashed lines hold for different interaction models (see section 5.2 of chapter 5). Data points from the Pierre Auger Observatory would appear in this plot somewhere between the blue and red lines, the proximity from one or another indicating a lighter or heavier composition at the corresponding energy (see the similar elongation rate plot presented in Chapter 3, Figure 3.3).

As anticipated in the first paragraph, we must specify that in the present state, only the *XAsymMax* parameter is retained for extracting composition. The *XAsymWidth* is excluded because of its low sensitivity to the primary mass as observed in Figure 4.6. As for the *AsymHeight* parameter, even though the correlation with X_{max} is good, its exclusion is related to a more fundamental issue of the Monte Carlo simulations in general. In fact it has been observed that the predicted amount of muons at ground level was not correctly reproduced by the Monte Carlo simulations. The height of the asymmetry longitudinal development *AsymHeight* was shown to be sensitive to this number of muons. Consequently, only the position of the maximum

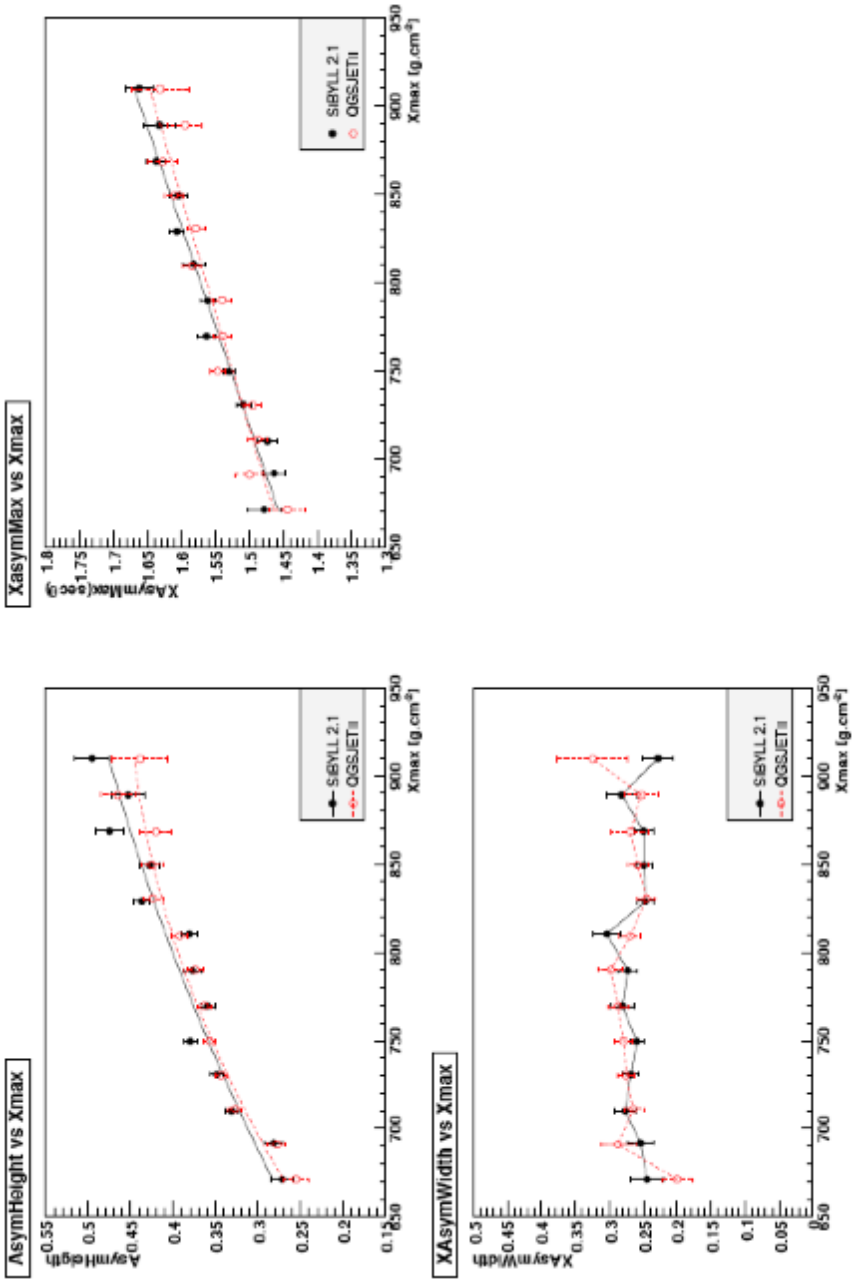

Figure 4.8: *Correlation of asymmetry parameters with the depth of shower maximum* X_{max}

of asymmetry is used for estimating the iron fraction as it remains weakly dependent on the number of muons at ground level and is on another hand weakly dependent on the value of the reconstructed energy. Finally, an important observation from Figure 4.6 and 4.8 is that the correlation of the asymmetry parameters with X_{max} and their dependence with primary composition is only weakly dependent on the hadronic interaction model used.

Chapter 5

Testing the Effect of de-convoluted Traces

There are different methods for mass composition studies also using as relevant experimental parameter the risetime parameter $t_{1/2}$. As mentioned in section 3.2.4, where we have described an alternative method using the fluctuations in $t_{1/2}$, it was found that the signals measured by the surface detectors of the Pierre Auger Observatory require to be corrected from inherent detector effects in order to recover the original time distributions of particles arriving in the detectors, thus minimizing fluctuations and improving the correlation with X_{max}, the main mass correlated parameter of a shower (see Chapter 3). A procedure of deconvolution is proposed, allowing to recover the original risetimes to an accuracy of 10%. The risetime $t_{1/2}$ is also the relevant experimental parameter of the method using the asymmetry parameters for mass composition estimation, but at present no correction is applied. The reason for this lies in the idea that the Monte Carlo simulations used in the method should also take such detector effects into account. Nevertheless, this calls for testing such an assumption and the effect of de-convoluted risetimes on the asymmetry method. In the first section we explain the deconvolution procedure used in University of Leeds, presenting the main results observed on the risetime. We refer to reference [18] for more information on the deconvolution procedure. We present in 5.2 a description of the Monte Carlo models that were used in this work and the specific set of cuts applied for the analysis. In section 5.3 we discuss the results of our own analysis applying deconvolution in the method using asymmetry parameters. Finally we studied the effects of using a different set of cuts on the analysis in 5.4.

5.1 De-convoluted Risetimes

5.1.1 The Detector Response Function

The *response function* of a detector is an important factor which is typically considered for the measurement of energy spectra of detected radiation. In the ideal case, a monoenergetic beam bombarding a detector should produce a Dirac delta function, i.e. a single output signal with fixed amplitude. However this is the ideal case and even a gaussian peak is not always realized depending on the type of radiation detected. The response function for a detector at a given energy depends on the different interactions the particles can undergo but also on the design and geometry of the detector.

The same issue is involved in the surface detectors of the PAO. Recalling the description of the detection techniques presented in chapter 2, the photomultipliers in each station detect photons diffused and reflected in the interior coating of the tanks. This forms what is called the"photon rattle". Effects of electronics and sampling in the photomultipliers also contribute to distort the response function. These effects together induce an exponential decay of the response function. Consequently, the traces measured are a convolution of the true time distributions of particles and the response function of each detector.

In the Pierre Auger Observatory, the average response function of the detectors for individual particles, the SPR(t) (the Single Particle Response), has been measured experimentally using atmospheric muons [30]. The measurement is done observing a peak in charge and pulse height histograms resulting from the signals in the PMTs (see Chapter 2, section 2.1.2 on the calibration procedures of the surface detectors). The following expression was obtained:

$$SPR(t) = A(e^{\frac{-t}{b}} - e^{\frac{-t}{a}}) \tag{5.1}$$

where values of a and b are known at the 10% level and were fixed at 67 ns and 13 ns respectively, these values computed by averaging different estimations. The SPR is constant for particles going through the detectors with inclinations lower than 60° and is similar for muons, electrons and photons. This is because the time it takes for these different particles to dissipate their energy in the detectors are much smaller than the typical values of this particular SPR, making impossible any disentanglement. The evaluated risetime is of 40ns and this defines a lower limit to the possible measurements.

One important consequence of this limit is that even though for large values of the risetime the limitation of the SPR is not a problem, for small values, time distributions for inclined showers are truncated at 40ns. This

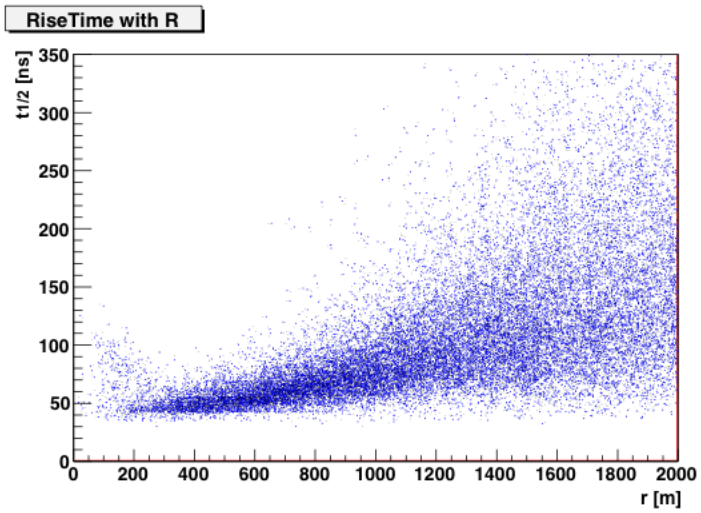

Figure 5.1: *Scatter plot of risetime values with the distance to the core. Events are selected for an angular range of* $59° < \theta < 62°$*, all energies mixed together. The expected lower limitation is clearly present around 40ns.*

effect is illustrated in Figure 5.1 where is presented a scatter plot of the values of risetimes with the distance to the core for a certain angle. We see that the distribution reaches a lower limit around 40ns.

5.1.2 The Deconvolution Algorithm

Formally, the general convolution product of two functions is mathematically expressed as:

$$(f * g)(x) = \int_{-\infty}^{+\infty} f(x-t) \cdot g(t)dt = \int_{-\infty}^{+\infty} f(t) \cdot g(x-t)dt \qquad (5.2)$$

For the discrete case of a system with N samples, equation 5.2 becomes:

$$(f * g)(n) = \sum_{n=-\infty}^{+\infty} f[n-m] \cdot g[m] = \sum_{n=-\infty}^{+\infty} f[m] \cdot g[n-m] \qquad (5.3)$$

The discrete case is appropriate for our study as the traces used to estimate the risetimes are recorded digitally. If we call $S(t)$ the output signal which is a convolution of the SPR and the arrival time distribution of the particles $x(t)$, then we can write:

$$S(t) = \sum_{\tau=0}^{N} SPR(t-\tau) \cdot x(\tau) \quad t = 0, 1, ..., 2N-1 \tag{5.4}$$

The arrival time distribution we are interested in is obtained by taking the inverse solution of equation 5.4, i.e.:

$$x(t) = S(0) - \frac{\sum_{\tau=1}^{N} SPR(t-\tau)x(\tau)}{SPR(0)} \tag{5.5}$$

The main issue with such solutions is their instability under small fluctuations in the input functions. As convoluted signals is a usual and well known problem in experimental physics, many technics have already been developed, having all different advantages. Here the GOLD deconvolution algorithm was chosen as it gives a positive and non oscillating solution [31].

The algorithm was applied to the initial traces in the detectors, $S(t)$, in order to extract de-convoluted values of the risetime. It was shown [18] that the differences in the risetimes (before and after applying the GOLD algorithm) were most important for inclined showers but nevertheless giving small but significant differences at all distances from the core and at all zenith angles. The effect of the deconvolution is illustrated in Figure 5.2, which was taken from [18]. As for the values of risetimes themselves, small values are strongly affected by the deconvolution while very small differences are observed for larger values, of the order of 350ns. The effect of deconvolution on risetimes of different values is the main feature which will explain the effects of the deconvolution procedure observed in the asymmetry analysis, see section 5.3.

The deconvolution procedure has been intensively studied to check for systematic effects and estimate the errors on the de-convoluted risetimes. In [18], it has also been demonstrated that even assuming a 30% uncertainty on the experimental measured SPR (this value holding only as an extreme bound), a more accurate estimation of the risetime is obtained using deconvolution, supporting the use of a deconvolution procedure for methods relying on the risetimes themselves rather than global features such as the azimuthal asymmetry, for instance. The 10% fluctuation in the SPR parameters a and b (equation 5.1) induces fluctuations of the order of 10 to 20% in the estimated risetimes. On another hand, the systematics effects resulting from this procedure also imply the use of tighter cuts than the ones used in the asymmetry method. The question of whether these highly selective cuts are also necessary when applying deconvolution in the asymmetry method

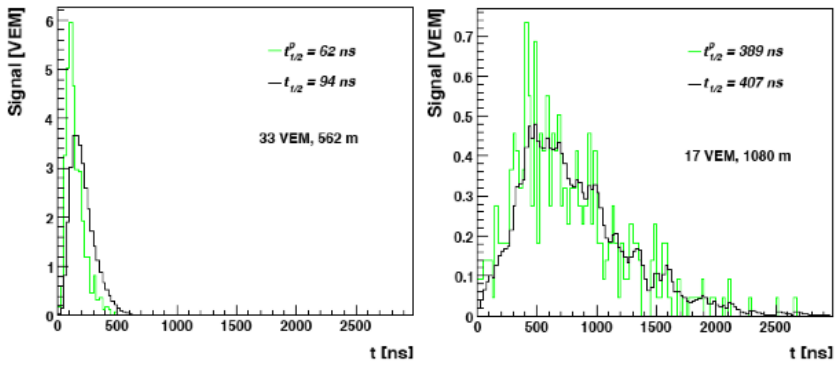

(a) (b)

Figure 5.2: *An example of traces obtained using the GOLD deconvolution algorithm. The left figure shows a trace simulated with the signal spread over a shorter period than the trace on the right. The fractional change in risetime between the original particle arrival distribution (green),* $t^p_{1/2}$*, and the convoluted trace (black),* $t_{1/2}$ *is much larger for the faster trace.*

is an important one, as tight cuts in signal and distance to the core tend to wash out the asymmetry. We discuss this issue in section 5.4.

5.2 Monte Carlo Simulations

5.2.1 Hadronic Interaction Models

The method presented in chapter 4 relies on hadronic interaction models, extrapolated from accelerator data at low energy. The reason for this is that there is no direct way of measuring composition from ultra high energy cosmic ray experiments and the development of the shower needs to be inferred by comparison with simulations. Gamma rays and neutrinos are well-known components of the cosmic ray flux in a wide range of energies but it is also known that these particles produce very characteristic signals that were not yet observed at the highest energies of the spectrum (see [32], [33] for the photon limit contribution and [34], [35] for the neutrino). The main contribution should thus be hadronic (more specifically baryons) and to study this, the most reasonable choice in a two component scenario is to consider the lightest species, the proton, and the most stable nucleus, iron. Such a model will give results indicating wether composition is light or heavy at the highest energy. Other methods can then be considered to study composition in more

details, for instance using models involving more than two components or simply other elements.

The results presented in the next section were obtained using Monte Carlo simulations performed with the AIRES code [36] using the hadronic interaction models QGSJETII(03) [37] and SIBYLL 2.1 [38]. The generated showers are used as input in the detector simulation code and finally reconstructed with the official offline reconstruction framework of the Pierre Auger Observatory [39]. Such a procedure is long and very complex. The main source of uncertainties for mass composition remains in the lack of knowledge we have in the hadronic interactions at the highest energies, as there is no accelerator data at these energies. Our understanding of the behaviors of the models at high energy should be improved with future data coming from the LHC experiment. However, this issue explains why we use different models where different methods of extrapolation are considered, giving slightly different results when predicting the shower parameters.

5.2.2 Event Selection

The cuts defined in the asymmetry analysis are mainly justified by the necessity of signals in detectors to be sensitive enough to the azimuthal asymmetry. As we have seen, this asymmetry does not occur for vertical showers and disappears for very inclined ones. The energy and zenith angle values used are the following:

- $log_{10}(E/eV) = 18.3, 18.7, 19.1, 19.3, 19.7, 19.9, 20.1$;
- $\theta(deg) = 32, 36, 41, 45, 49, 53, 57, 60, 63$

The range of θ values is the one for which the asymmetry is shown to be the most sensitive to the shower evolution.

Some quality cuts are applied to remove badly reconstructed events. On the SD stations, a $0.5 < R < 2.0$ km cut was applied to the distance of the stations from the core. The lower bound $R > 0.5$ km was chosen to avoid saturation problems as the high density of particles close to the core can induce very high signals in the tanks. On the other hand, the $R < 2.0$ km cut removes highly fluctuating signals and assures the stations are inside the region for which the risetime grows linearly with core distance (see [40]). Finally a cut on the signal itself is applied, $S > 10$ VEM to reject stations where the signal is not clean enough to allow well reconstructed values of $t_{1/2}$.

These cuts have been studied in detail in [41] and shown to be optimum in the present method for separating primary masses, considering both efficiency and the discriminating power. In section 5.4, some other cuts were considered, following the analysis in [18]. They introduced some systematic effects originating from a loss of sensitivity to the asymmetry and a important loss of statistics, supporting the use of the cuts described here.

5.3 Effect of Deconvolution in the Asymmetry Analysis

5.3.1 Risetime Distributions

After generating the set of de-convoluted risetimes using the deconvolution procedure put at our disposal by University of Leeds, our first step consisted in implementing the use of the new de-convoluted risetimes, $t^d_{1/2}$, in the asymmetry analysis. If a relevant effect of deconvolution on the asymmetry method was to be observed, then it is natural to think that such an effect could only come from the effect of $t^d_{1/2}$ in the first step of the analysis, i.e. in the time distribution asymmetries. Therefore, we followed the evolution of the effect of $t^d_{1/2}$ in each step of the analysis explained in the previous chapter to understand the resulting effect on the *XAsymMax* vs. *Energy* relation, last step before extracting the composition.

In Figure 5.3, we plot the azimuthal distributions corresponding to the proton QGSJETII model for different zenith angles for the convoluted case in the left plot and the de-convoluted one on the right. The behavior in both cases is the same, exhibiting the azimuthal asymmetry. Still a closer look shows the profiles change with deconvolution and become lower. Figure 5.4 shows the same plots for a real set of data of the Pierre Auger Observatory. We can see the distributions are similar for the data and also affected by deconvolution. To understand more precisely how the profiles are affected, we studied the difference of risetimes with azimuthal angle. This is shown in Figure 5.5 which only illustrates the discussion but must not be used to extract values of reference as the curves do not correspond to the same selection of events. The behavior of this difference can be explained by the fact that deconvolution affects more small values of $t_{1/2}$ than larger ones (see section 5.1.2). Therefore the difference between the risetimes is greater in the late region (where the electromagnetic particles are more absorbed across the array) than in the early one. This means that the azimuthal asymmetry increases with deconvolution. The negative contributions in the differences

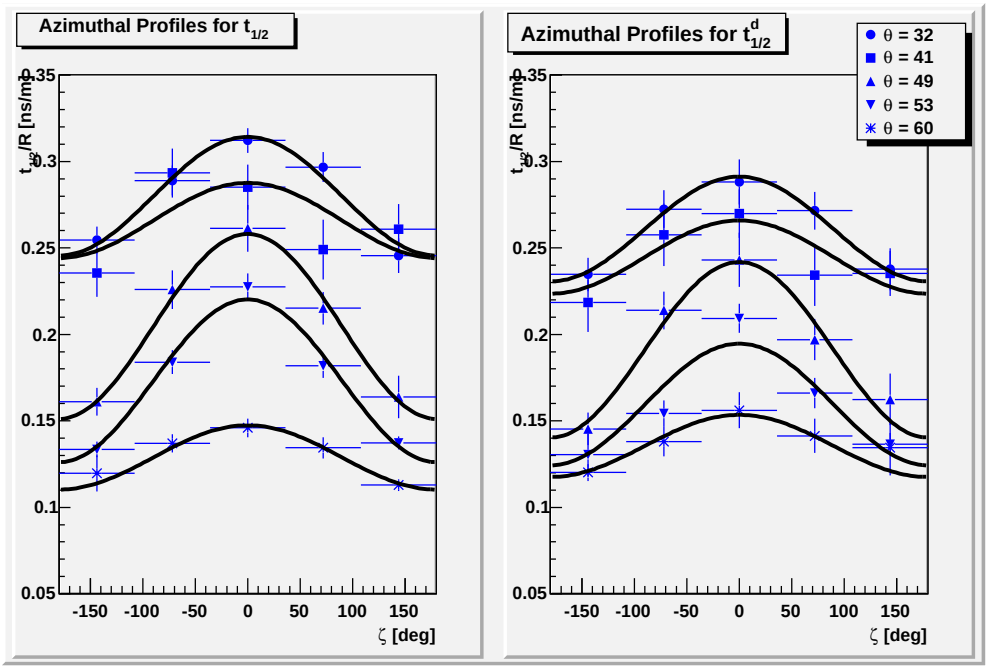

Figure 5.3: *Risetime distributions with azimuthal angle for the convoluted (left) and de-convoluted (right) case for a chosen energy of* $10^{18.5} eV$. *The behavior is the same, showing an azimuthal asymmetry at all angles. Nevertheless, it can be seen that the distributions themselves are flattened by deconvolution, indicating an effect on the asymmetry itself.*

for small angles come from cases where the deconvolution gives higher values of $t^d_{1/2}$ than $t_{1/2}$. This was shown to occur mainly for stations far away from the core of the shower. This is because with growing energy, the muon component becomes much faster than the electromagnetic one, as expected, but this one is also more affected by multiple scattering for stations far from the core. These effects are seen to result in higher de-convoluted risetimes (than the convoluted counterparts). Thus negative contributions disappear with more inclined showers, again because deconvolution affects mainly small values of $t_{1/2}$ (as the electromagnetic component is almost completely absorbed for very inclined showers). It can also be seen that the difference increases with zenith angle which means the difference between asymmetries extracted from the convoluted and de-convoluted cases will also increase. Finally, we should expect this difference between asymmetries to decrease for very high zenith angles. In fact, the azimuthal asymmetry basically disappears for very inclined showers and thus all values of risetime, even though being very small, are affected equally by deconvolution, at all ζ values.

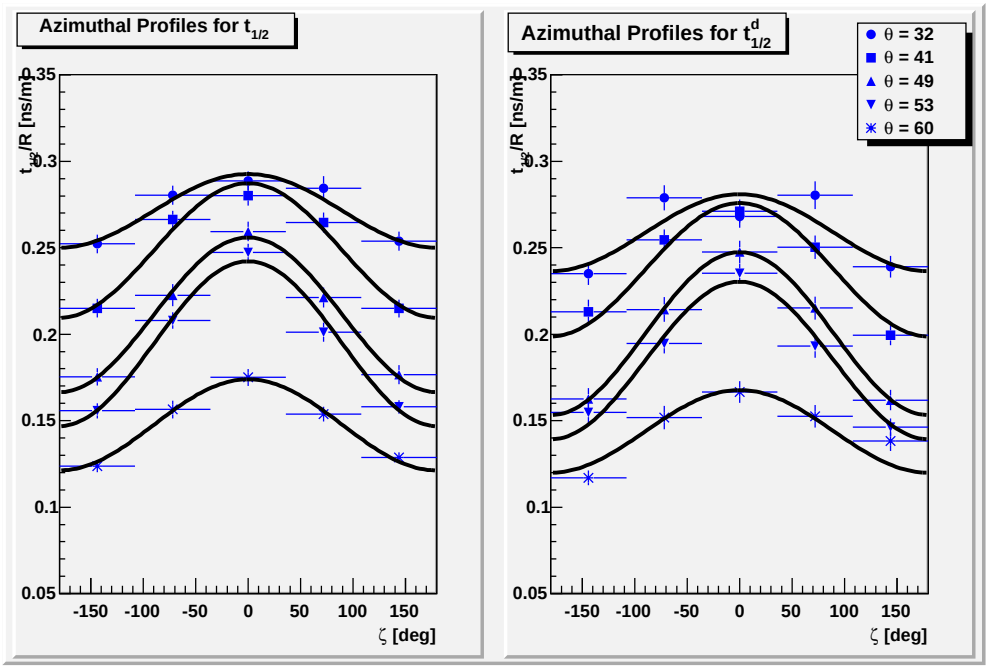

Figure 5.4: *Same as Figure 5.3 but this time for a real set of data. We can see the profiles are similar for data and behave the same way under deconvolution.*

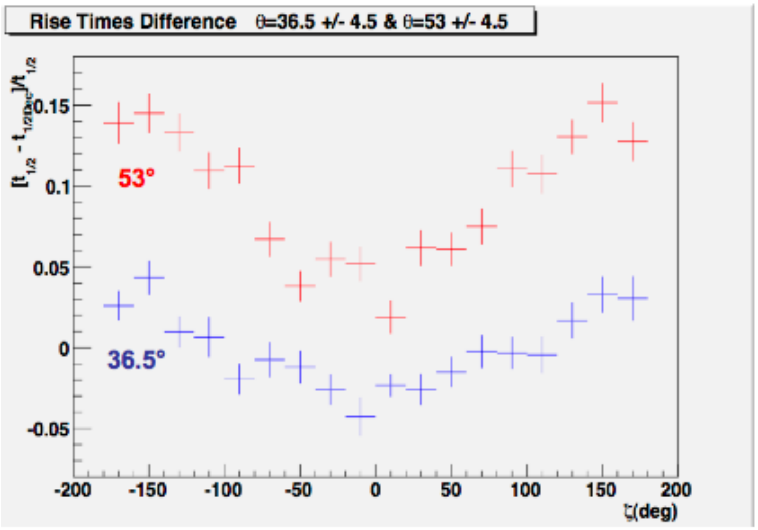

Figure 5.5: *Normalize difference* $(t_{1/2} - t^d_{1/2})/t_{1/2}$ *versus azimuthal angle. Deconvolution affects more small values of the risetime, dominant in the late region of the shower plane* ($\zeta = +and - \pi$). *We also notice the difference increases with zenith angle.*

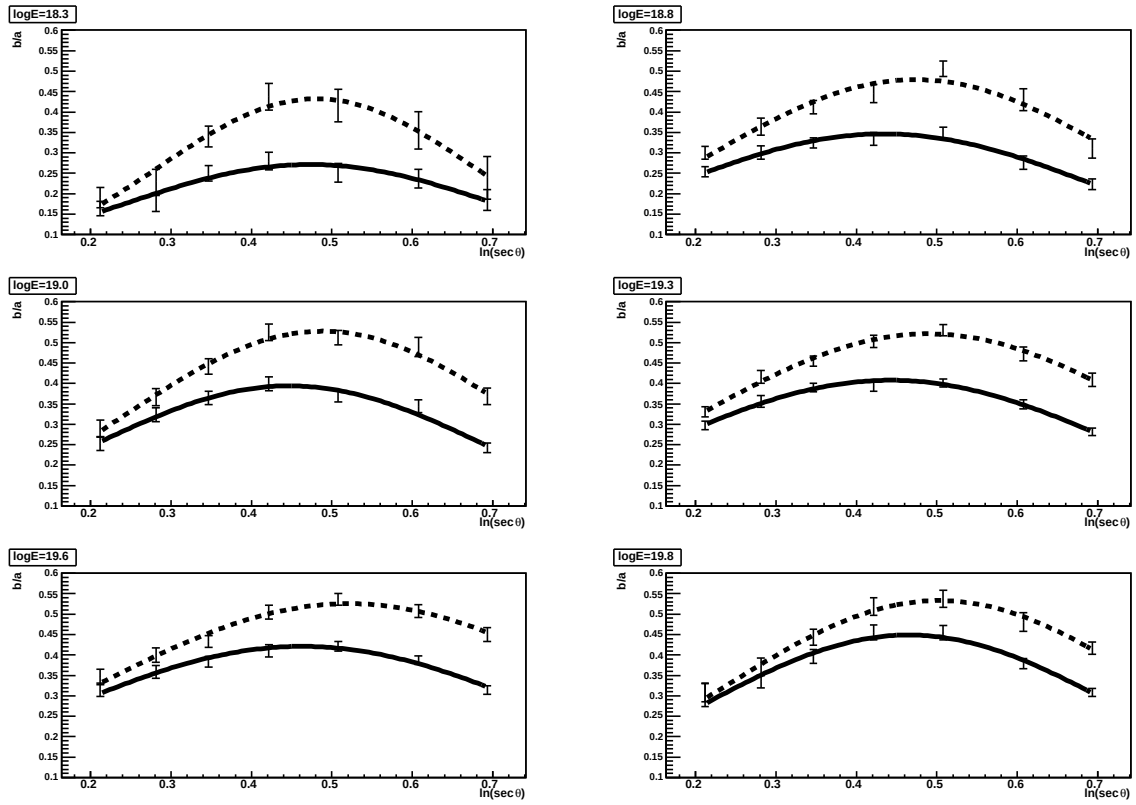

Figure 5.6: *Longitudinal asymmetry development for convoluted (solid lines) and de-convoluted (dashed lines) risetimes. It can be observed that the de-convoluted results always show higher values of asymmetry, the differences increasing with the inclination of the shower (see text for more details). The results presented here correspond to the proton QGSJETII(3.0) case.*

All these effects appear clearly in the longitudinal asymmetry development presented in Figure 5.6. At low zenith angles, the difference between the extracted asymmetries is small but becomes bigger for more inclined showers. The fact that this difference should also decrease for very high angles (because the azimuthal asymmetry basically disappears for both convoluted and de-convoluted risetimes) is less clear because our cuts limit the zenith angle to a maximum value of 60°. Still the overall behavior is clearly manifest for the lowest energy plot and for the reasons given above, we can expect it to be the same for all other energies. The results of Figure 5.6 corresponds to a proton case simulated with the QGSJETII model. The same behavior has been observed for all other simulated cases and also for data. On another example is given in Figure 5.7 for the QGSJETII iron case.

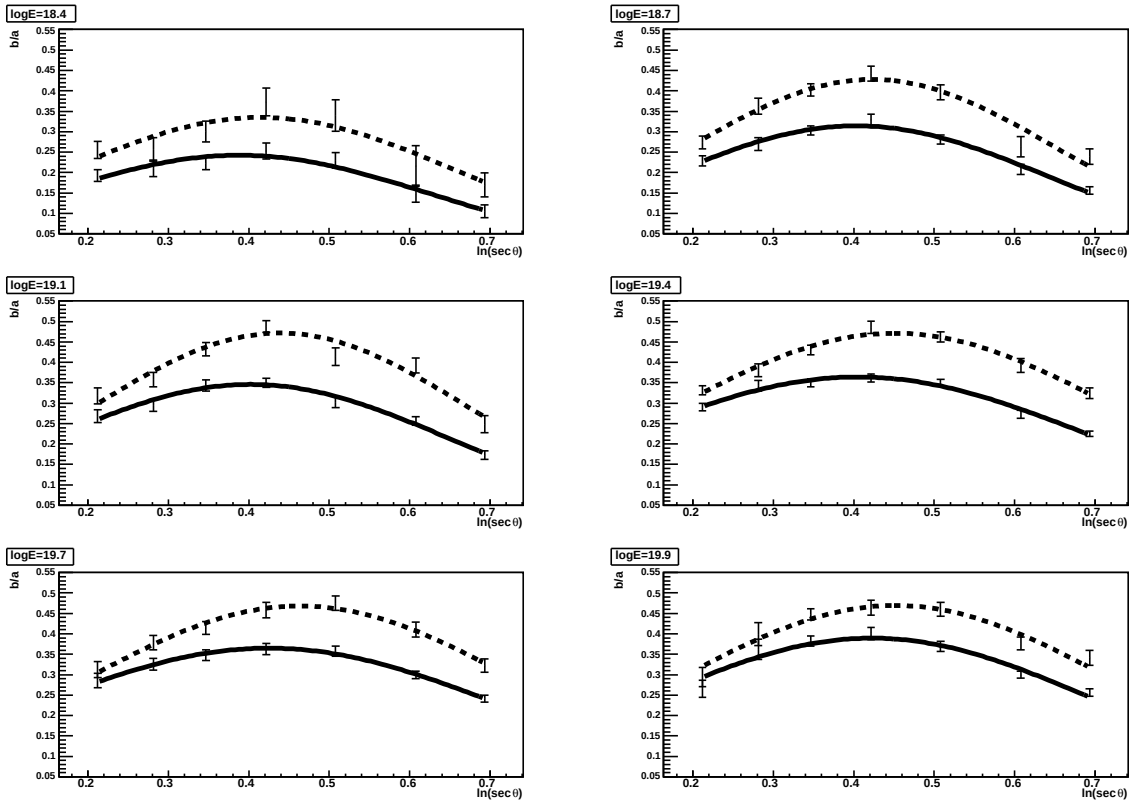

Figure 5.7: *Same comments as for Figure 5.6, here for the iron QGSJET(3.0) case.*

$log_{10}(E[eV])$	XAsymMax	$XAsymMax^d$	Relative Difference [%]
18.3	1.562 [±0.017]	1.569 [±0.017]	0.4 [±0.02]
18.8	1.556 [±0.013]	1.610 [±0.016]	3.4 [±0.2]
19.0	1.556 [±0.012]	1.608 [±0.015]	3.2 [±0.1]
19.3	1.556 [±0.009]	1.628 [±0.013]	4.4 [±0.2]
19.6	1.582 [±0.011]	1.672 [±0.018]	5.4 [±0.3]
19.7	1.609 [±0.008]	1.649 [±0.014]	2.4 [±0.3]

Table 5.1: *Values of* XAsymMax *before and after deconvolution. The last column shows the relative difference.*

5.3.2 The Position of Maximum of Asymmetry

The effects of deconvolution on the values of asymmetries extracted from the azimuthal time distributions are well understood. However, it is not straightforward to predict the effect on the relevant parameter for mass composition, the position of maximum of asymmetry *XAsymMax*. More subtle than the effect on asymmetry values themselves is the way the gaussian fit to the longitudinal profile is affected. From the longitudinal profiles presented in Figure 5.6, we see that the gaussian fits change with deconvolution. But more important is the fact that the position of the maximum of asymmetry also changes.

Table 5.1 presents the values of *XAsymMax* extracted from the longitudinal profiles of Figure 5.6 for the convoluted and de-convoluted cases. As can be seen, there is a systematic shift of the position of the maximum of asymmetry towards higher values. Also, looking at Figure 5.8 which presents the relative differences of *XAsymMax* values between the convoluted and deconvoluted case, it seems there is a trend for an increasing effect with energy, except for the last energy bin. However, in Figure 5.8, the value of the difference in the last energy bin is already presented using a slightly different computation in the analysis, adding an extra bin at high theta values (from 62° to 63°). In fact it was observed that the longitudinal fit was improved using this inclusion, and most important, the difference between the convoluted and de-convoluted values of *XAsymMax* increases. This could indicate that using different ranges and numbers of bins for each energy can improve the fits of the longitudinal profiles. This is an important result but implementing such a procedure in the standard analysis is not straightforward and this should be considered for future work. The point to make here is that there seems to be indeed an increasing effect of deconvolution with energy, as shown in Figure 5.6.

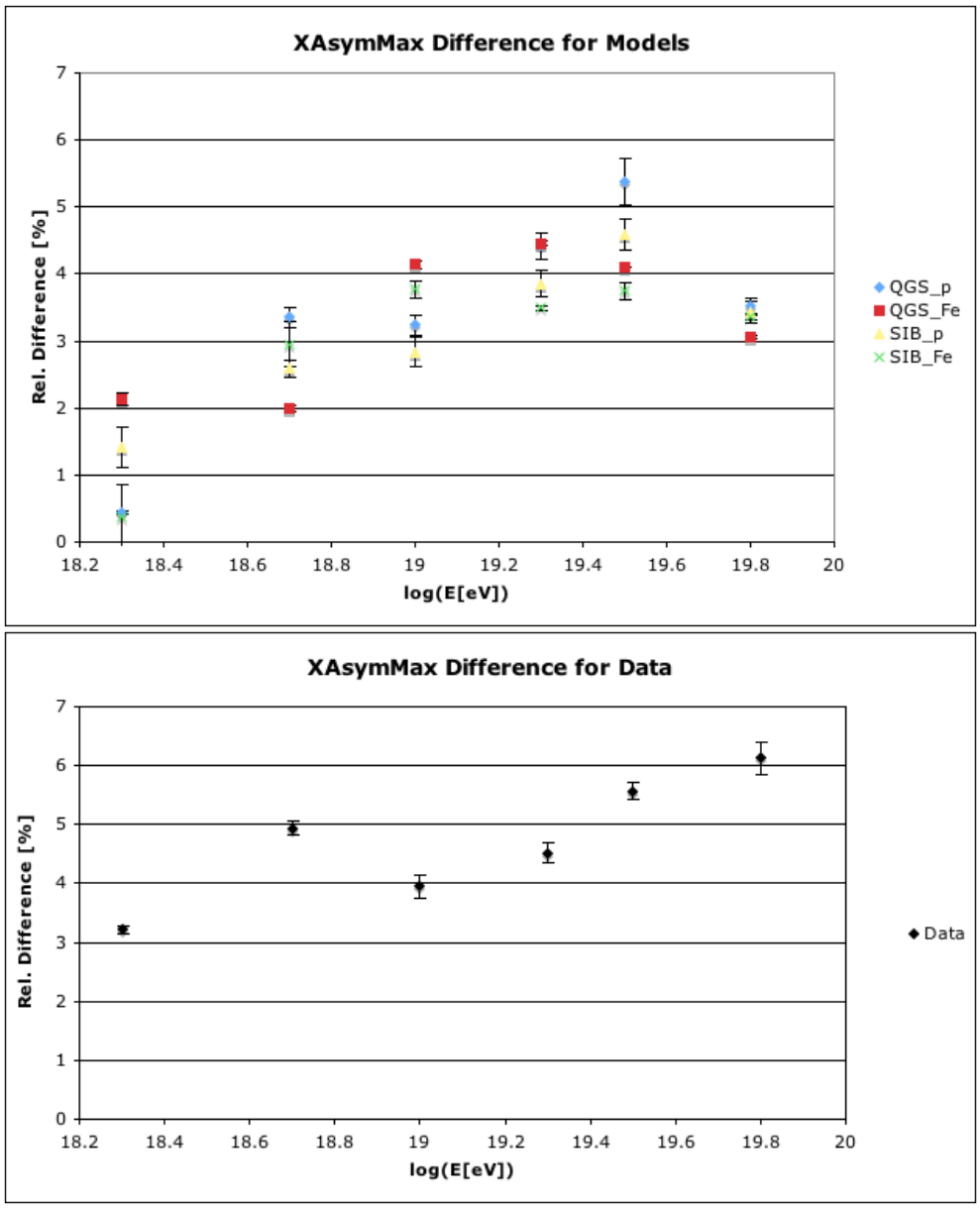

Figure 5.8: *Relative Difference of* XAsymMax *values for convoluted and de-convoluted risetimes. The effect of deconvolution increases with energy, except for the last energy bin in the Monte Carlo simulations. See text for more information.*

To understand better the dependence of deconvolution with energy, additional studies are needed. Looking at the behavior of the values of the deconvoluted risetimes, we observed that for core distances higher than 1000m, there was a tendency of de-convoluted risetime values being always larger than their convoluted counterparts. Such cases are well understood but the fact that this effect is systematic over a certain distance from the core and also over certain values of the risetime is not. Also this effect was observed to increase with energy, the difference between $t_{1/2}$ and $t^d_{1/2}$ becoming greater and values of risetimes after deconvolution being always larger. Perhaps this could explain the dependence of deconvolution with energy we observe in the resulting values of *XAsymMax*. There is no physical reason for the first effect. Thus no conclusion can be drawn for the moment and a more precise understanding of the deconvolution procedure has to be considered.

The last step consists in analysing how the general *XAsymMax* relation with energy is affected by deconvolution. Examples for both models (QGSJETII on the left and SIBYLL on the right) are presented in Figure 5.9. Again, our aim here is to look at the behavior of the fits under deconvolution. The systematic shift of the position of maximum of asymmetry induced by deconvolution is clearly visible for both primaries, the resulting fits being shifted upwards. However, we can also observe the dependence of deconvolution with energy, as the slopes of the fits are also slightly increased after deconvolution. Recalling the picture of how composition is extracted from these plots, it is obvious that the observed change in the behavior of the fits can have a strong effect on composition. We can only know if this is the case by plotting de-convoluted results for data. Unfortunately, this right was not given to us by the Pierre Auger Collaboration at the present time. We can only stress that from the previous step of our analysis, data appeared to be affected in the same way than the models and that within errors, convoluted and de-convoluted results for composition are compatible.

5.4 Effect of Different Cuts

Studying the effects of different cuts in the asymmetry analysis was motivated by the fact the alternative method discussed in section 3.2.4, chapter 3, exploiting the fluctuations in the risetime parameter, and in which was explained the importance of using a deconvolution procedure, uses a different set of cuts. Of course, both methods use different features of the risetime. Essentially, the asymmetry analysis is more of a statistical nature, requiring larger cuts to keep samples of events of sufficient size. However the cuts are

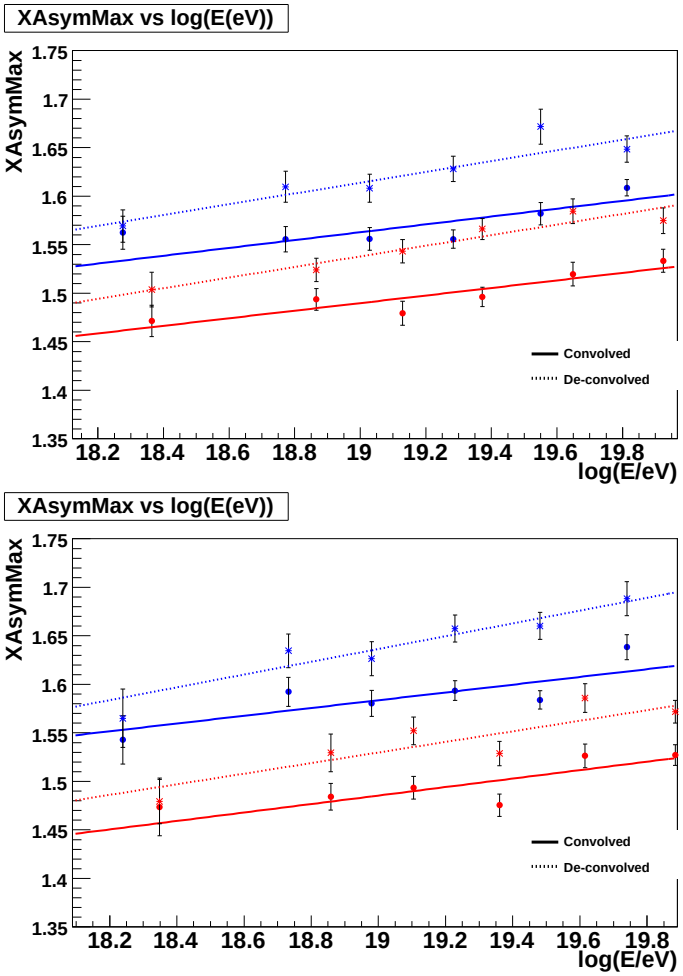

Figure 5.9: *Effect of deconvolution on the* XAsymMax *values with energy. Dashed lines and star markers represent the de-convoluted results, blue being proton and red iron (QGSJETII(3.0) on the left, SIBYLL 2.1 on the right). The systematic shift towards higher values of XAsymMax is clearly seen and also a significant change in the slope due to the dependence of deconvolution with energy.*

Cuts	Method 1	Method 2
S [VEM]	> 10	> 20
R[m]	$500 < R < 2000$	$600 < R < 1400$
θ	$< 62°$	$< 45°$

Table 5.2: *Different cuts for the method using the asymmetry method (Method 1) and the method using the mean value of X_{max} and its fluctuations (Method 2).*

neither arbitrary and demand a high sensitivity to the azimuthal asymmetry characteristic of the arrival time distributions of particles. The chosen cuts have already been described in section 5.2.2. As for the alternative method using the fluctuations in the risetime parameter, it relies on an event by event analysis, thus demanding tighter cuts to select high quality samples allowing for precise estimations of the relevant parameters. Using the deconvolution procedure in the asymmetry analysis called for testing the effects of tighter cuts, as the ones used in the alternative method. The main relevant cuts of both methods which were tested are presented in Table 5.2.

The cut on the θ angle would obviously make us loose the features of the asymmetry needed for our analysis. Furthermore, this cut has very little to do with the deconvolution procedure itself which supports the idea of neglecting it here. Thus we concentrated the rest of our work on the study of cuts applied to the signal in the stations, S, and the distance to the core R. Instead of going through each step of the analysis like in the previous section, we present here directly the effect observed on the relation of the position of maximum of asymmetry with energy, which is the primary composition estimator. This is shown in Figure 5.10. The left plot corresponds to the de-convoluted case using the cuts of the asymmetry analysis. In the right plot are presented the results for the new set of cuts (Table 5.2). It is clear there is an effect induced by the cuts, apparently affecting more the SIBYLL Monte Carlo model. Later, we show that this effect is stronger for SIBYLL because of a lack of statistics present at low energies for this model compared to QGSJETII (and thus not because of some feature inherent to SIBYLL).

To understand the effects induced by the new cuts, we studied separately the cut on the signal and the distance to the core, thus making a study of the systematics induced by the cuts on *XAsymMax*. We used steps in the values of the cuts, going from $S > 10$VEM to $S > 20$VEM by steps of 2 VEM and from $500 < R < 2000$m to $600 < R < 1400$m by steps of 200m [1]. In Figures

[1] Actually, steps of 100m were considered but the same results came out in both cases.

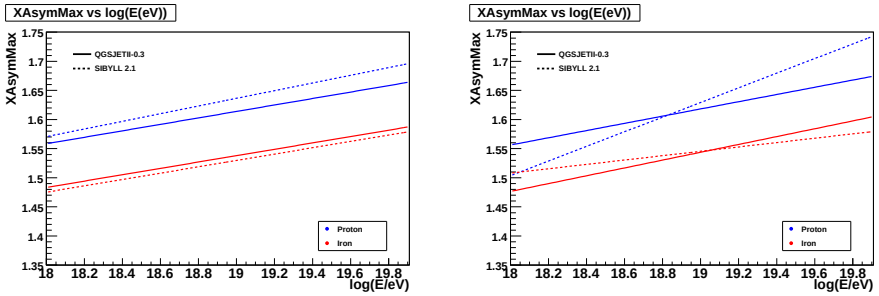

Figure 5.10: *Elongation rates of the* XAsymMax *parameter for different sets of cuts on the signal and the distance to the core. The left plot corresponds to the normal cuts used in the asymmerty analysis,* $S > 10\,VEM$ *and* $500 < R < 2000m$ *while the right plot holds for cuts* $S > 20\,VEM$ *and* $600 < R < 1400$.

5.11 and 5.12, we show the effects of growing cuts on the *XAsymMax* values (top plots) presented with the corresponding losses of events, in %, in each energy bin (bottom plots).

For the signal cut, no specific trend can be observed except in the first energy bin. As expected, we loose more events at low energy as showers of lower energies tend to induce smaller signals at the detection level. Cutting at higher values of the signal basically removes stations far from the core and more sensitive to the azimuthal asymmetry. This explains why the values in the first energy bin decreases with the successive cuts.

For the cuts on the distance to the core (Figure 5.12), again the first energy bin is significantly affected, this time showing a trend of values growing with the cuts. For all other energies, only statistical fluctuations due to the loss of events with the cuts are involved. It can also be observed that cutting stations far from the core removes high energy signals while cutting on the lower bound affects the low energy region.

Finally, neglecting the effect in the first energy bin (where the loss of statistics is important), we can conclude that there is a systematic error on *XAsymMax* of the order of 5% due to reasonable variations of the cuts on the signal and the distance to the core. This reflects a good stability and reproducibility of the results under the tested cuts.

In general, the results for proton are less stable under the cuts than the ones for iron. First, looking at the actual number of events, less showers were simulated for the proton case in the first energy bin, the loss of statistics having thus a stronger effect. However, in general, the proton simulations are more sensitive to the cuts because protons induce showers with particular characteristics in the signal which are more affected by the cuts.

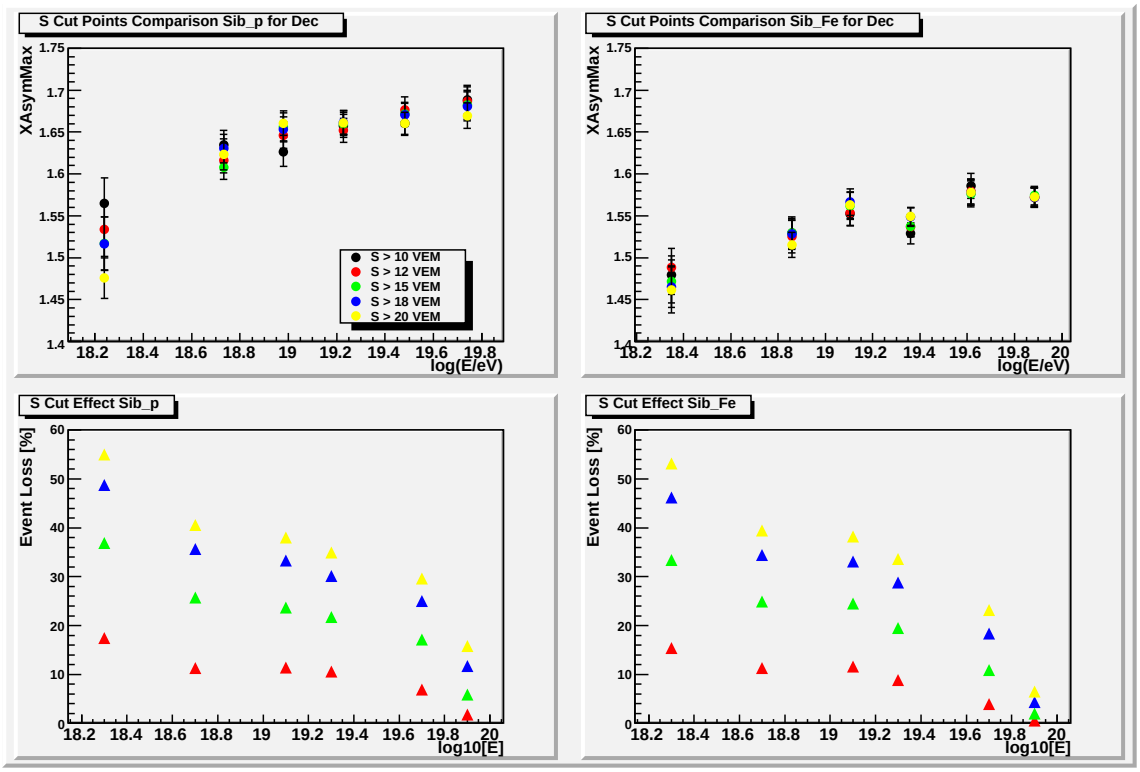

Figure 5.11: *Effect of increasing values of the signal cut on the* XAsymMax *parameter. The down plots show the corresponding losses of events after each cut in each energy bin.*

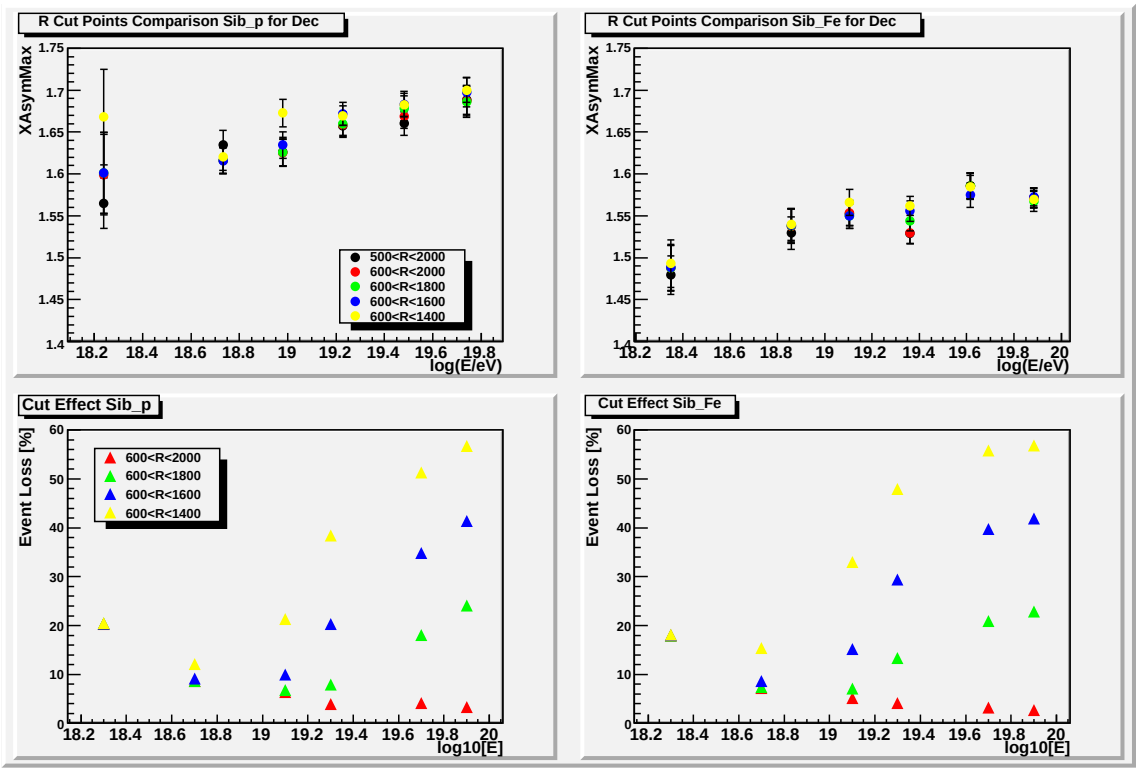

Figure 5.12: *Effect of increasing values of the R cut on the* XAsymMax *parameter. The down plots show the corresponding losses of events after each cut in each energy bin.*

If we consider the combined effect of both cuts, we see in Figure 5.13 that the loss in statistics becomes very important. In the low energy region, it is a sum of the losses induced by the signal cut and distance to the core cut separately. At high energy, the loss is the one of the distance to the core cut meaning both cuts remove the same stations at high energy. The resulting effect in the low energy bin is of course very important, as expected since we loose more than 70% of statistics and most important, sensitivity to the asymmetry due to the signal cut. For the other energies, the small fluctuations lead to an estimation of systematic errors on the $XAsymMax$ value of not more than 5%. This means only the effect in the lowest energy bin should affect significantly the fits of the elongation rate in Figure 5.10. As for the cut on the distance to the core, certainly it has strong statistical effects but no systematic effects seem to be involved. In conclusion, this means the signal cut is as expected the most important cut for the asymmetry analysis and needs to be maintained at the value of 10 VEM which was shown to be optimum for sensitivity to the azimuthal asymmetry. The R cut essentially removes a lot of statistics from the analysis without introducing any observable systematic effect. As more statistics are obtained, this should become even more clear.

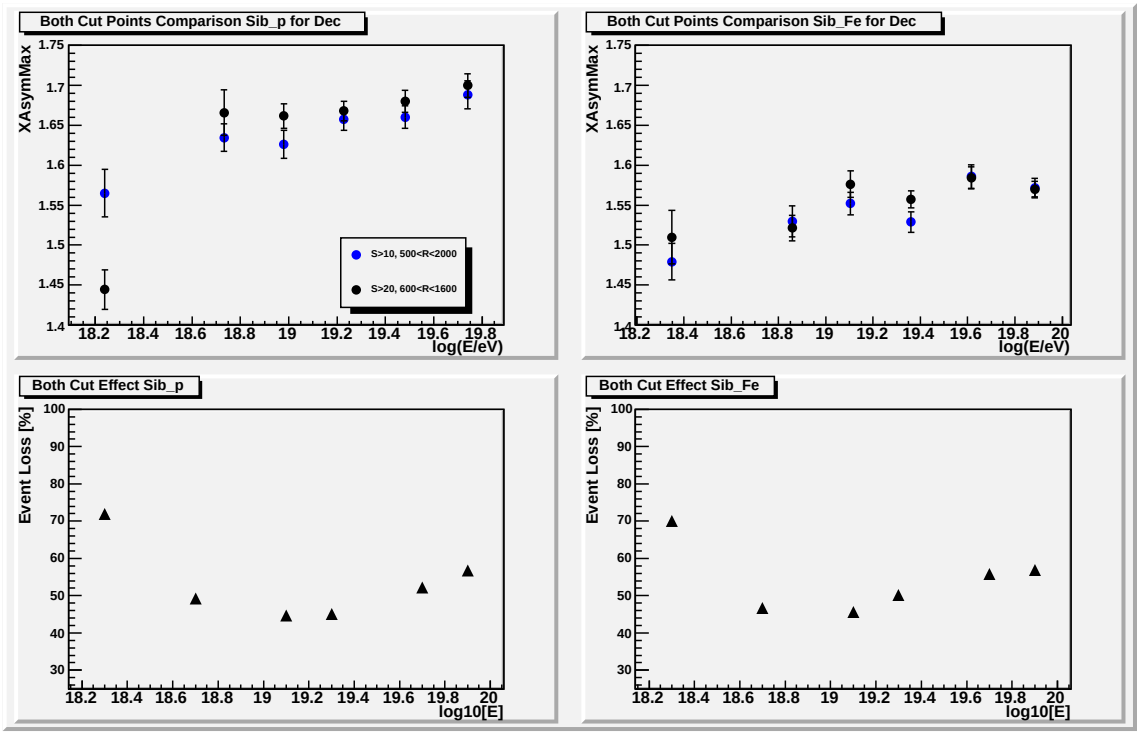

Figure 5.13: *Combined effect of both cuts on the* XAsymMax *values for the SIBYLL model. Only the low energy bin is significantly affected by the cuts, this being explained on one hand by a considerable loss of statistics (see down plots) and by a loss of sensitivity to the asymmetry due to the signal cut, lowering the values of asymmetry.*

Chapter 6

Conclusion

Our lack of knowledge of mass composition at ultra high energies has become an issue that can no longer be ignored. The method presented here, using the asymmetry in the time distributions of particles at ground, is a novel and very promising method. In this work we have studied the effect of using time distributions previously corrected from inherent detector effects on the general analysis, concentrating on Monte Carlo simulations.

It was observed that using a deconvolution procedure induces a shift in the values of the position of maximum of asymmetry, $XAsymMax$, the relevant mass estimator. The fact that all extracted values are larger in the de-convoluted case is explained by the features of the deconvolution procedure itself, small values of the risetime being more strongly affected. In addition to this, it was observed that this effect also increases with energy, resulting in a small change in the behavior of the relation of the position of maximum of asymmetry with energy compared to the convoluted case. These effects of deconvolution were shown to affect the simulations and the data in the same way. Therefore we expect the results on composition not to be affected by deconvolution. This has already been checked for the lowest energies where results are compatible within errors. At the highest energies the lack of statistics in the data sample prevents any conclusion. Finally we studied the effects induced by different cuts. Cutting on higher values of the signal was found to introduce a loss of sensitivity to the asymmetry, supporting the initial cut established for the analysis. Cuts in the distance to the core mainly consisted in an important loss of statistics.

At present, it seems that the choice of using a deconvolution procedure in the asymmetry method does not introduce any relevant changes in mass composition determination using the position of maximum of asymmetry as the estimator. However, it is clear that deconvolution affects the asymmetry

profiles and it is worth considering the question whether more information can be extracted from the use of time distributions closer to reality, when using the whole longitudinal asymmetry distribution as a mass estimator. At present, the dependence of deconvolution with energy is something we do not fully understand and is the most important issue that should be addressed for future work.

Bibliography

[1] M. Nagano and A. A. Watson. Observations and implications of ultrahigh-energy cosmic rays. *Reviews of Modern Physics*, 72(3), July 2000.

[2] Peter K.F. Grieder. *Cosmic Rays at Earth.* Elsevier, 2001.

[3] Luis Anchordoqui et al. High energy physics in the atmosphere: Phenomenology of cosmic ray air showers. *Ann. Phys.*, 314:145–207, 2004.

[4] T. Antoni and al. Kaskade experiment. *Astropart. Phys.*, 24, September September 2005.

[5] R. J. Protheroe. Origin and propagation of the highest energy cosmic rays. 1996.

[6] J. Abraham et al. Observation of the suppression of the flux of cosmic rays above 4×10^{19}eV. *Phys. Rev. Lett.*, 101:061101, 2008.

[7] R.U. Abbasi and al. *Physical Review Letters*, 100(101101), 2008.

[8] James W. Cronin. The highest-energy cosmic rays. *Nucl. Phys. Proc. Suppl.*, 138:465–491, 2005.

[9] Enrico Fermi. On the Origin of the Cosmic Radiation. *Phys. Rev.*, 75:1169–1174, 1949.

[10] C. F. Kennel and al. *J. Geophys. Res.*, 91:917, 1986.

[11] P. O. Lagage and C. J. Cesarsky. The maximum energy of cosmic rays accelerated by supernova shocks. *Astron. Astrophys.*, 125:249–257, 1983.

[12] L. Oc. Drury. An introduction to the theory of diffusive shock acceleration of energetic particles in tenuous plasmas. *Rept. Prog. Phys.*, 46:973–1027, 1983.

[13] The Pierre Auger Collaboration. The pierre auger observatory design report. Technical report, March 1997.

[14] C. Wileman. *The Spread in Arrival Times of Particles in Air-Showers for Photon and Anisotropy Searches above 10 EeV.* PhD thesis, University of Leeds, 2008.

[15] The Pierre Auger Collaboration. *Astropart. Phys.*, pages 243–256, May 2008.

[16] J. Abraham et al. Correlation of the highest energy cosmic rays with nearby extragalactic objects. *Science*, 318:938–943, 2007.

[17] R. U. Abbasi et al. Search for Correlations between HiRes Stereo Events and Active Galactic Nuclei. *Astropart. Phys.*, 30:175–179, 2008.

[18] B. E. Smith. *The Mass Composition of Cosmic Rays Above 1 EeV Inferred Using the Spread in Arrival Times of Air Shower Particles.* PhD thesis, University of Leeds, 2008.

[19] D. Allard, N. G Busca, G. Decerprit, A. V. Olinto, and E. Parizot. Implications of the cosmic ray spectrum for the mass composition at the highest energies. *JCAP*, 0810:033, 2008.

[20] A.M. Hillas, D.J. Marsden, H.W. Hollows, and H.W. Hunter. 3:1001, 1971.

[21] David Newton, J. Knapp, and A. A. Watson. The optimum distance at which to determine the size of a giant air shower. *Astropart. Phys.*, 26:414–419, 2007.

[22] R. Knapik et al. The Absolute, Relative and Multi-Wavelength Calibration of the Pierre Auger Observatory Fluorescence Detectors. 2007.

[23] J. Linsley. In *15th ICRC*, volume 12, page 89, Plovdiv, 1977.

[24] Proc. 28th ICRC. Number 401, Tokyo, 2003. Universal Academy Press.

[25] A.J. Baxter. *Properties of extensive air showers deduced from the shower fronts.* PhD thesis, University of Leeds, 1967.

[26] P. Bassi, G. Glark, and B. Rossi. *Phys. Rev.*, 92:441–451, October 1953.

[27] A. A. Watson and J.G. Wilson. *Journal of Physics A Mathematical General*, 7:1199–1212, July 1974.

[28] L.N. Epele M.T. Dova and A.G. Mariazzi. *Astroparticle Physics*, 18, 2003.

[29] M. T. Dova, H. Wahlberg, and al. Time asymmetries in extensive air showers: a novel method to identify UHECR species. 2009.

[30] M. Aglietta et al. Response of the Pierre Auger Observatory water Cherenkov detectors to muons. Presented at 29th International Cosmic Ray Conference (ICRC 2005), Pune, India, 3-11 Aug 2005.

[31] R. Argonne National Laboratory. Gold. *ANL*, 9684, 1964.

[32] The Pierre Auger Collaboration. *Astroparticle Physics*, 29:243–256, May 2008.

[33] J. Abraham et al. Upper limit on the cosmic-ray photon flux above 10^{19} eV using the surface detector of the Pierre Auger Observatory. *Astropart. Phys.*, 29:243–256, 2008.

[34] The Pierre Auger Collaboration. *Physical Review Letters*, 100, February 2008.

[35] J. Abraham et al. Upper limit on the diffuse flux of UHE tau neutrinos from the Pierre Auger Observatory. *Phys. Rev. Lett.*, 100:211101, 2008.

[36] S.J. Sciutto. Airshower extended simulations. *arXiv:astro-ph/9911331*, 1999.

[37] S. Ostapchenko. *Nucl. Phys. Proc. Suppl.*, B 151:143, 2006.

[38] *Proc. 26th International Cosmic Ray Conference*, Utah, USA, 1999.

[39] S. Argiro al. *Nuclear Instrum. Meth.*, A 580:1485, 2007.

[40] A. A. Watson J.G. Wilson R. Walker. *Journal of Physics G Nuclear Physics*, 7:1297–1309, September 1981.

[41] Pinto Diego Garcia. *Time Asymetry in UHE Cosmic Ray Showers. Mass Composition Studies in the Pierre Auger Observatory.* PhD thesis, Universidad Complutense de Madrid, 2009.

[42] G. S. H. Wilkens. *Experimental study of high energy muons from Extensive Air Showers in the energy range 100 TeV to 10 PeV.* PhD thesis, Katholieke Universiteit Nijmegen, July 2003.

[43] Maximo Ave. A study of very inclined showers in the Pierre Auger Observatory. 2003.

[44] P. Privitera. The angular reconstruction and angular resolution of air showers detected at the Auger Observatory. Prepared for 28th International Cosmic Ray Conferences (ICRC 2003), Tsukuba, Japan, 31 Jul - 7 Aug 2003.

[45] R. Walker and A. A. Watson. Measurement of the elongation rate of extensive air showers produced by primary cosmic rays of energy above 2x $10^1 7eV. J.Phys., G7 : 1297 - -1309, 1981$.

[46] M. T. Dova. The Pierre Auger Observatory. *Nucl. Phys. Proc. Suppl.*, 122:170–178, 2003.

[47] M. T. Dova. Survey of the Pierre Auger Observatory. To be published in the proceedings of 27th International Cosmic Ray Conference (ICRC 2001), Hamburg, Germany, 7-15 Aug 2001.

[48] J. A. Bellido and for the Pierre Auger Collaboration. Mass Composition Studies of the Highest Energy Cosmic Rays. 2009.

[49] Johannes Bluemer and for the Pierre Auger Collaboration. The Pierre Auger Observatory: Results on Ultra-High Energy Cosmic Rays. 2008.

[50] C. Bonifazi and for the Pierre Auger Collaboration. The angular resolution of the Pierre Auger Observatory. 2009.

[51] The Pierre Auger Collaboration. Limit on the diffuse flux of ultra-high energy tau neutrinos with the surface detector of the Pierre Auger Observatory. 2009.

[52] The Pierre Auger Collaboration. Upper limit on the cosmic-ray photon fraction at EeV energies from the Pierre Auger Observatory. 2009.

[53] Carlos Hojvat and for the Pierre Auger Collaboration. The Pierre Auger Cosmic Ray Observatory, Comments on Recent Results. 2008.

[54] Silvia Mollerach and for the Pierre Auger Collaboration. Search for clustering of ultra high energy cosmic rays from the Pierre Auger Observatory. 2009.

[55] M. Risse and for the Pierre Auger Collaboration. Search for photons at the Pierre Auger Observatory. 2009.

[56] Michael Unger and for the Pierre Auger Collaboration. Composition Studies with the Pierre Auger Observatory. 2009.

[57] Esteban Roulet and for the Pierre Auger Collaboration. Recent results from the Pierre Auger Observatory. *J. Phys. Conf. Ser.*, 136:022051, 2008.

[58] Fabian Schmidt and for the Pierre Auger Collaboration. Measurements of the Muon Content of UHECR Air Showers with the Pierre Auger Observatory. 2009.

[59] Serguei Vorobiov and for the Pierre Auger Collaboration. The Pierre Auger Observatory - a new stage in the study of the ultra-high energy cosmic rays. 2008.

[60] L. Wiencke and for the Pierre Auger Collaboration. Atmospheric Calorimetry above 10^{19} eV: Shooting Lasers at the Pierre Auger Cosmic-Ray Observatory. *J. Phys. Conf. Ser.*, 160:012037, 2009.

[61] M. Aglietta et al. Anisotropy studies around the galactic centre at EeV energies with the Auger observatory. *Astropart. Phys.*, 27:244–253, 2007.

[62] J. Abraham et al. Correlation of the highest-energy cosmic rays with the positions of nearby active galactic nuclei. *Astropart. Phys.*, 29:188–204, 2008.

[63] Maria Teresa Dova and Sergio Ferrari. Confronting models on cosmic ray interactions with particle physics at LHC energies. *Eur. Phys. J.*, C52:673–681, 2007.

[64] R. U. Abbasi et al. Measurement of the Flux of Ultra High Energy Cosmic Rays by the Stereo Technique. 2009.

[65] C. Bleve. Indirect measurements of cosmic rays. *Nuovo Cim.*, 123B:912–914, 2008.

[66] J. Bluemer, R. Engel, and J. R. Hoerandel. Cosmic Rays from the Knee to the Highest Energies. 2009.

[67] Glennys R. Farrar, Andreas A. Berlind, and Ingyin Zaw. Correlations between Ultrahigh Energy Cosmic Rays and Infrared-Luminous Galaxies. 2009.

[68] V. Dogiel and D. Breitschwerdt. Cosmic Rays in the Disk and Halo of Galaxies. 2009.

[69] Glennys R. Farrar, Ingyin Zaw, and Andreas A. Berlind. Correlations between Ultrahigh Energy Cosmic Rays and AGNs. 2009.

[70] A. V. Glushkov. Problem of the energy spectrum of ultrahigh-energy cosmic rays. *Phys. Atom. Nucl.*, 72:85–96, 2009.

[71] P. Lipari. Gammas, neutrinos and cosmic rays. *Nuovo Cim.*, 123B:695–700, 2008.

[72] J. F. Ormes and J. F. Arens. Calorimeters for Cosmic Rays. Paper published in the Proceedings of the Calorimeter Workshop, 9-10 May 1975, Fermilab, Batavia, IL.